

Enhancement in ionic conductivity of Dysprosium doped $\text{Li}_7\text{La}_3\text{Zr}_2\text{O}_{12}$ solid electrolyte applied in Li-ion batteries

By

Hamed Salimkhani

Submitted to the Graduate School of Engineering and Natural Sciences in partial fulfillment of the requirements for the degree of Master of Science

Sabanci University August 2020

Enhancement in ionic conductivity of Dysprosium doped $\text{Li}_7\text{La}_3\text{Zr}_2\text{O}_{12}$ solid electrolyte applied in Li-ion

APPROVED BY:

Prof. Dr. Selmiye Alkan Gürsel
(Thesis Supervisor)



Asst. Prof. Dr. Alp Yürüm
(Thesis Co-supervisor)



Prof. Dr. Mehmet Ali Gülgün



Prof. Dr. Adem Tekin



Assoc. Prof. Dr. Emre Erdem



Assoc. Prof. Dr. Önder Metin



DATE OF APPROVAL: 25/8/2020

©2020 by Hamed Salimkhani

ALL RIGHTS RESERVED

Enhancement in ionic conductivity of Dysprosium doped $\text{Li}_7\text{La}_3\text{Zr}_2\text{O}_{12}$ solid electrolyte applied in Li-ion batteries

Hamed Salimkhani

Materials Science and Nano-Engineering, MSc Thesis, 2020

Supervisor: Prof. Dr. Selmiye Alkan Gürsel

Keywords: LLZO, Dysprosium, Dopant, XRD, Ionic conductivity, Solid-state MAS NMR

Abstract: In this investigation, a novel Li-stuffed garnet type solid electrolyte with enhanced properties was fabricated. For this purpose, different concentrations of Dy ranging from 0.1 to 0.8 atoms per formula unit (pfu) were doped into the $\text{Li}_7\text{La}_3\text{Zr}_2\text{O}_{12}$ to stabilize the cubic structure and, therefore, tailor the ionic conductivity. Furthermore, fundamental studies were performed through X-ray diffraction and Rietveld refinement to develop crystal structure of the Dy doped LLZO and determine the site preference of Dy. On another attempt in this study, Density Functional (DFT) total energy computations were applied to investigate the convergence of Dy at different Wyckoff sites energetically and to further validate the results of experiments. Additionally, ^7Li and ^6Li solid-state MAS NMR was performed to reveal the chemical coordination of Li at different sites. The results of this thesis project indicated that Dy ions probably substitute for Zr site and Li ions prefer tetrahedral (24d) and octahedral (48g) atomic sites. Additionally, our novel solid electrolyte demonstrated the highest ionic conductivity ($2.03 \times 10^{-3} \text{ S.cm}^{-1}$) reported for LLZOs.

Li-ion pillerde uygulanan Disprosyum katkılı $\text{Li}_7\text{La}_3\text{Zr}_2\text{O}_{12}$ katı elektrolitin iyonik iletkenliğinde artış

Hamed Salimkhani

Malzeme Bilimi ve Mühendisliği, MSc Tezi, 2020 Tez
Danışmanı: Prof. Dr. Selmiye Alkan Gürsel

Anahtar Kelimeler: LLZO, Disprozyum, Katkılama, XIK, iyonik iletkenlik, Katı Hal MAS NMR

Özet: Bu araştırmada geliştirilmiş özelliklere sahip Li barındıran garnet tipi yeni bir katı elektrolit üretildi. Bu amaçla, kübik yapıyı stabilize etmek ve dolayısıyla iyonik iletkenliği ayarlamak için $\text{Li}_7\text{La}_3\text{Zr}_2\text{O}_{12}$ formül birimi (pfu) başına 0.1 ila 0.8 atom arasında değişen farklı Dy konsantrasyonlarıyla katkılıdır. Dahası, Dy katkılı LLZO'nun kristal yapısını geliştirmek ve Dy'nin yer tercihini belirlemek için X-ışını kırınımı ve Rietveld iyileştirme kullanılarak temel çalışmalar yapıldı. Öte yandan bu çalışmada Dy'nin farklı Wyckoff bölgelerinde enerjisel olarak yakınsamasını araştırmak ve deney sonuçlarını daha ileri düzeyde doğrulamak için yoğunluk fonksiyonel teorisi ile (DFT) toplam enerji uyarlamaları uygulandı. Ek olarak, farklı konumlardan Li'nin kimyasal çevresini göstermek için ^7Li and ^6Li katı hal MAS NMR kullanıldı. Bu tez çalışmasının sonuçları ile Dy'nin muhtemel olarak Zr ile yer değiştirdiği ve Li iyonlarının tetrahedral (24d) ve oktahedral (48g) bölgelerine yerleştiği belirtildi. Ek olarak, yeni katı elektrolitimiz LLZO'lar şimdiye kadar rapor edilen en yüksek iyonik iletkenliği ($2.03 \times 10^{-3} \text{ S.cm}^{-1}$) sahip olduğunu gösterdi.

Acknowledgment

In this thesis, all the DFT computational studies were performed by Prof. Dr. Adem Tekin and Dr. Riccarda Caputo using the computing resources provided by the National Center for High Performance Computing of Turkey (UHEM), under Grant No. 1002132012 at Istanbul Technical University. I would like to thank Prof. Dr. Adem Tekin and Dr. Riccarda Caputo for their selfless efforts and supports throughout my thesis.

I would like to gratefully thank my supervisor and co-supervisor, Prof. Selmiye Alkan Gürsel and Dr. Alp Yurum without whom I could not complete this research, and without whom I would not have made it through my master's degree. Their support was limitless which I owe them all my success now and then.

I would like to thank all my defense jury members for their constructive review and comments on my thesis.

Finally, yet importantly, I would like to adore my beautiful wife and my lovely parents for their huge support in these two years.

Dedication

I would like to dedicate this thesis to my wife and my mother.

Table of Contents

Abstract

Özet

Acknowledgment

Table of Contents

List of Figures

1. Introduction.....	2
1.1. General information.....	3
1.2. Structure of LLZO garnet.....	4
1.3. Defect chemistry in LLZO.....	7
1.3.1. Intrinsic.....	7
1.3.1.1. Vacancies.....	7
1.3.1.2. Interstitial.....	8
1.3.2. Extrinsic.....	9
1.3.2.1. Substitutional impurity.....	9
1.4. Impact of various dopants on the Li ⁺ ion transport of LLZO.....	10
1.4.1. Effect of Al ³⁺	10
1.4.2. Effect of Ta ⁵⁺ and Nb ⁵⁺	13
1.4.3. Effect of Ge ⁴⁺	17
1.4.4. Effect of Ga ³⁺	19
1.4.5. Effect of Sb ⁵⁺	21
1.4.6. Effect of Fe ³⁺	23
1.5. Solid-state NMR theory.....	25
1.5.1. Zeeman Interaction.....	26
1.5.2. Direct Dipole-Dipole interaction.....	26
1.5.3. J-coupling.....	27
1.5.4. Chemical Shift.....	27
1.5.5. Quadrupole interaction.....	28
1.5.6. ⁷ Li and ⁶ Li spectra of LLZO.....	28
1.5.7. ²⁷ Al, ¹³⁹ La, ⁷¹ Ga, ⁴⁵ Sc and ¹⁷ O spectra.....	30
1.6. Electrochemical Impedance Spectroscopy of LLZOs (EIS).....	33
2. Objectives of this thesis.....	40
3. Materials and methods.....	42
3.1. Synthesis.....	43
3.2. Computational method.....	43
3.3. Characterization.....	44
3.3.1. PXRD.....	44
3.3.2. MAS NMR.....	44
3.3.3. FESEM.....	45
3.3.4. ICP.....	45

3.3.5. EIS.....	45
4. Results and discussions.....	46
4.1.PXRD of samples.....	47
4.2.Dy-substitute LLZO.....	49
4.3.Bonding features.....	52
4.4. ⁷ Li and ⁶ Li MAS NMR.....	56
4.5.Ionic conductivity measurements.....	59
5. Conclusions.....	64
References.....	65

List of Figures

Figure 1. Polyhedral model of general $A_3B_3C_2O_{12}$ garnet crystal structure.....	5
Figure 2. Polyhedral models of a) #230 and b) #220 space groups in garnet type LLZO crystal structure.....	5
Figure 3. Representation of a pair of Schottky defect.....	8
Figure 4. Representation of a pair of Frenkel defect.....	9
Figure 5. Polyhedral model of Al^{3+} doped LLZO crystal structure.....	12
Figure 6. Impact of Al^{3+} content on crystallinity and purity of the cubic phase.....	13
Figure 7. Polyhedral model of Ta^{5+}/Nb^{5+} doped LLZO crystal structure.....	14
Figure 8. XRD patterns of LLZO doped with various concentrations of Nb^{5+}	16
Figure 9. XRD patterns of LLZO doped with various concentrations of Ta^{5+}	16
Figure 10. Polyhedral model of Ge^{4+} doped LLZO crystal structure.....	18
Figure 11. XRD patterns of LLZO doped with various concentrations of Ge^{4+}	18
Figure 12. Representation of a) Centric cubic structure with a space group of $Ia\bar{3}d$ (no.230). b) Centric cubic structure with a space group of $I\bar{4}3d$ (no.220). c) Li-ion pathway of $Ia\bar{3}d$ (no.230). d) Li ion pathway of $I\bar{4}3d$ (no.230).....	20
Figure 13. XRD patterns of Ga^{3+} doped LLZO with various concentrations of Ga^{3+}	21
Figure 14. Polyhedral model of Sb doped LLZO crystal structure.....	21
Figure 15. XRD patterns of LLZO doped with various concentrations of Sb^{5+}	23
Figure 16. Polyhedral model of Fe^{3+} doped LLZO crystal structure with acentric SG $I\bar{4}3d$ (No.220).....	24
Figure 17. XRD patterns of LLZO doped with various concentrations of Fe^{3+}	25
Figure 18. demonstrates 7Li NMR spectra recorded by an old NMR device (10T).....	29
Figure 19. 7Li NMR spectra recorded by a new NMR device (21T).....	29
Figure 20. ^{27}Al MAS NMR spectra of Al^{3+} doped LLZO.....	31
Figure 21. Experimental and simulated ^{139}La MAS NMR spectra of $LaLi_{0.5}Fe_{0.2}O_{2.09}$ structure.....	31
Figure 22. ^{71}Ga MAS NMR spectra of Ga^{3+} doped LLZO.....	32
Figure 23. ^{45}Sc MAS NMR spectra of Sc^{3+}/Ga^{3+} doped LLZO.....	32
Figure 24. ^{17}O MAS NMR spectra of Al^{3+}/Ga^{3+} doped LLZO.....	33
Figure 25. schematic of Randle's circuit with the bulk (R_b) and grain boundary (R_{gb}) resistance are shown on it.....	34
Figure 26. Impedance spectra of Fe^{3+} doped LLZO at various temperatures.....	39

Figure 27. (a) X-ray powder diffraction patterns of $\text{Li}_7\text{La}_3\text{Dy}_x\text{Zr}_{2-x}\text{O}_{12}$ at different composition. (b) The impurity phase diffraction peaks occurring at high Dy content, assigned to the formation of pyrochlore phase $\text{La}_2\text{Zr}_2\text{O}_7$	47
Figure 28. Variation of lattice parameter as a function of Dy content in $\text{Li}_7\text{La}_3\text{Dy}_x\text{Zr}_{2-x}\text{O}_{12}$	50
Figure 29. Experimental and calculated patterns of $\text{Li}_7\text{La}_3\text{Dy}_x\text{Zr}_{2-x}\text{O}_{12}$ at $x=0.2$ from rietveld refinement...	51
Figure 30. demonstrates the polyhedral model of Dy-LLZO structure.....	52
Figure 31. The band structure and the partial density of states of undoped LLZO.....	53
Figure 32. The band structure and the partial density of states of Dy doped LLZO.....	53
Figure 33. Projected density of states of undoped LLZO.....	54
Figure 34. Projected density of states of Dy doped LLZO. An isodensity surface showing the f-p character of the Dy-O bonding is shown in the Dy-PDOS panel.....	55
Figure 35. ^7Li MAS NMR spectrum of $\text{Li}_7\text{La}_3\text{Dy}_x\text{Zr}_{2-x}\text{O}_{12}$ at $x=0.2$ recorded at 273 K.....	57
Figure 36. (a) The MAS ^6Li NMR spectrum of $\text{Li}_7\text{La}_3\text{Dy}_x\text{Zr}_{2-x}\text{O}_{12}$ at $x=0.2$ at 273 K. (b) The deconvoluted partial MAS NMR spectrum of ^6Li	58
Figure 37. T_1 relaxations curve of ^7Li for $x=0.2$ at 273 K.....	59
Figure 38. EIS spectra of $\text{Li}_7\text{La}_3\text{Dy}_x\text{Zr}_{2-x}\text{O}_{12}$ at (a) $x=0.1$, (b) $x=0.2$, (c) $x=0.4$, and (d) $x=0.8$	61
Figure 39. Fitted plot impedance spectrum along with equivalent circuit for $\text{Li}_7\text{La}_3\text{Dy}_x\text{Zr}_{2-x}\text{O}_{12}$ at $x=0.2$	62
Figure 40. Effect of Dy content on the ionic conductivity of LLZO.....	62

List of Tables

Table 1. Crystallographic information of S.G #230.....	5
Table 2. Crystallographic information of S.G #220.....	6
Table 3. Summary of the ionic conductivities of aliovalent doped LLZOs.....	37
Table 4. Standard enthalpies of formation for different compounds of this work derived from DFT computations.....	49
Table 5. Coordination, occupancy, thermal factor and site preference of different atoms for LLZO at x=0.2 pfu are demonstrated.....	51
Table 6. Calculated ionic conductivities for Dy=0.1, 0.2, 0.4, and 0.8 pfu in LLZO through fitting of EIS spectra by equivalent circuit.....	60

Introduction

1. Introduction

1.1. General information

The demand for cleaner and cheaper portable energy resources has never stopped during the last decades. On the other hand, by the development of novel energy storage devices, safety has been the priority of researchers and companies in their projects. When for the first time high energy lithium-ion batteries were fabricated, they were thought to be harmless to consumers until explosions occurred [1, 2]. This failure in such useful batteries changed the trend of the development of these energy storage devices. Hence, a new generation of Li-ion batteries emerged known as all solid lithium ion batteries [3]. Like other energy storage devices, these batteries can also find applications in portable electronic devices and electric vehicles such as smartphones and cars due to their higher energy densities [4], safety [5], and better cyclic performances [6]. The emergence of these batteries has somehow been able to solve the problems arising from the liquid nature of the electrolyte of conventional lithium-ion batteries. Like all other batteries, all solid state Li-ion batteries are composed of two electrodes and an electrolyte in between. However, in this case, the nature of the electrolyte between the two electrodes is solid. The task of an electrolyte in a Li-ion battery is to transport (conduct) Li ions from the cathode to the anode or vice versa in which the electrolyte plays an important role in this scenario. The term ‘‘Ionic Conductivity’’ is the keyword that none of the battery researchers can avoid in their research. A solid electrolyte with a higher ionic conductivity is the first prerequisite for having a better all solid state Li-ion battery. Therefore, the choice of proper material to produce a solid electrolyte is the key to develop a Li-ion battery with superior properties and higher safety. Recent advances in this field have introduced many different applicable materials to this area such as Li garnet-type $\text{Li}_7\text{La}_3\text{Zr}_2\text{O}_{12}$ (LLZO) [7]. The LLZO was first introduced by Murugan et al [8] as an excellent candidate for a solid electrolyte due to its better Li ion transport properties [9], better interfacial stability with the electrode [10], higher mechanical property [11, 12] and excellent performance at higher temperatures [13]. In the following sections, we will have a review of recent advances in this area along with familiarizing the reader with the structure and effect of different dopants on properties of LLZOs.

1.2. Structure of LLZO garnet

The general structure of garnet is given as $\text{A}_3\text{B}_3\text{C}_2\text{O}_{12}$; where A, B, and C refer to divalent and trivalent and tetravalent cations, respectively (shown in **Figure 1**) [14]. This structure is composed of a framework in which A cations are located in 8 fold-coordinated sites, B cations in 6 fold-coordinated sites and C cations are located in 4 fold-coordinated sites. This configuration is composed of the tetrahedral 24d-A sites linked by an octahedral 16a-B having a common face with each of the two neighbors 24d-A sites. A face-sharing site, three tetrahedral A and six bridging octahedral sites account for 9 sites per formula unit which lowers the activation energy for the movement of Li^+ ions if they are disordered with partial occupancies of both sites [15, 16].

In the case of LLZO structure, there are two distinct known polymorphs, Tetragonal, and Cubic [17]. The tetragonal structure is composed of a framework having two kinds of 8-fold LaO_8 coordination (8b and 16e) and 6-fold ZrO_6 coordination (16c). Additionally, Li^+ ions are allowed to take tetrahedral 8a, octahedral 16f, and 32g sites [18]. On the other hand, a cubic phase comes into two polymorphs; namely centric SG $\text{Ia}\bar{3}\text{d}$ (No.230) and acentric SG $\text{I}\bar{4}3\text{d}$ (No.220). The SG $\text{Ia}\bar{3}\text{d}$ (No.230) has a structure with La ions coordinated with eight oxygen atoms located at 24c Wyckoff position and with Zr ions coordinated with six oxygen atoms located at 16a Wyckoff position [19]. Moreover, SG $\text{I}\bar{4}3\text{d}$ (No.220) has a structure with La ions coordinated with eight oxygen atoms located at 24d Wyckoff position and with Zr ions coordinated with six oxygen atoms located at 16c Wyckoff [20]. Li^+ ions can prefer various sites in both structures. For instance, 96h, 24d and 48g Wyckoff positions are possible sites for Li^+ ions to occupy in SG $\text{Ia}\bar{3}\text{d}$ (No.220) [21] and 12a, 12b and 48e Wyckoff positions can be occupied by Li^+ in SG $\text{I}\bar{4}3\text{d}$ (No.220). **Table 1** and 2 demonstrate all the possible Wyckoff positions, coordinates, and site symmetry of both SG $\text{Ia}\bar{3}\text{d}$ (No.220) and SG $\text{I}\bar{4}3\text{d}$ (No.220), respectively. Additionally, **Figure 2a&b** demonstrate polyhedral model of both #230 and #220 structures.

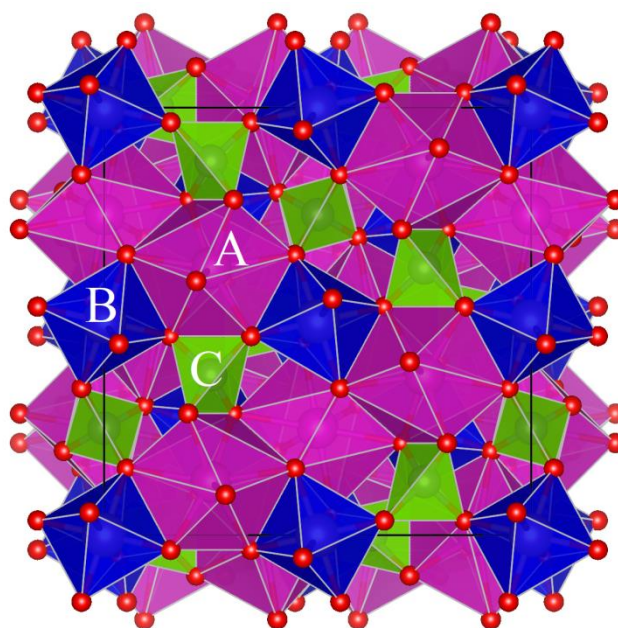


Figure 1. Polyhedral model of general $\text{A}_3\text{B}_3\text{C}_2\text{O}_{12}$ garnet crystal structure.

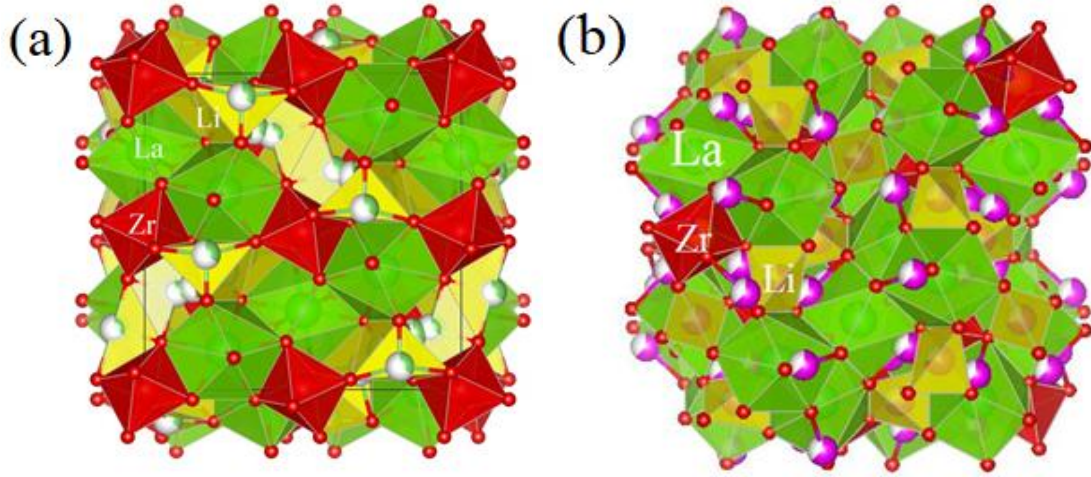


Figure 2. Polyhedral models of a) #230 and b) #220 space groups in garnet type LLZO crystal structure.

Table 1. Crystallographic information of S.G #230 [22].

Multiplicity	Wyckoff letter	Site symmetry	Coordinates			
			$(0,0,0) + (1/2,1/2,1/2) +$			
96	H	1	(x,y,z) (z,x,y) (y,z,x) $(y+3/4,x+1/4,-z+1/4)$ $(x+3/4,z+1/4,-y+1/4)$ $(z+3/4,y+1/4,-x+1/4)$ $(-x,-y,-z)$ $(-z,-x,-y)$ $(-y,-z,-x)$ $(-y+1/4,-x+3/4,z+3/4)$ $(-x+1/4,-z+3/4,y+3/4)$ $(-z+1/4,-y+3/4,x+3/4)$	$(-x+1/2,-y,z+1/2)$ $(z+1/2,-x+1/2,-y)$ $(-y,z+1/2,-x+1/2)$ $(-y+3/4,-x+3/4,-z+3/4)$ $(-x+1/4,z+3/4,y+1/4)$ $(z+1/4,-y+1/4,x+3/4)$ $(x+1/2,y,-z+1/2)$ $(-z+1/2,x+1/2,y)$ $(y,-z+1/2,x+1/2)$ $(y+1/4,x+1/4,z+1/4)$ $(x+3/4,-z+1/4,-y+3/4)$ $(-z+3/4,y+3/4,-x+1/4)$	$(-x,y+1/2,-z+1/2)$ $(-z+1/2,-x,y+1/2)$ $(y+1/2,-z+1/2,-x)$ $(y+1/4,-x+1/4,z+3/4)$ $(-x+3/4,-z+3/4,-y+3/4)$ $(-z+1/4,y+3/4,x+1/4)$ $(x,-y+1/2,z+1/2)$ $(z+1/2,x,-y+1/2)$ $(-y+1/2,z+1/2,x)$ $(-y+3/4,x+3/4,-z+1/4)$ $(x+1/4,z+1/4,y+1/4)$ $(z+3/4,-y+1/4,-x+3/4)$	$(x+1/2,-y+1/2,-z)$ $(-z,x+1/2,-y+1/2)$ $(-y+1/2,-z,x+1/2)$ $(-y+1/4,x+3/4,z+1/4)$ $(x+1/4,-z+1/4,y+3/4)$ $(-z+3/4,-y+3/4,-x+3/4)$ $(-x+1/2,y+1/2,z)$ $(z,-x+1/2,y+1/2)$ $(y+1/2,z,-x+1/2)$ $(y+3/4,-x+1/4,-z+3/4)$ $(-x+3/4,z+3/4,-y+1/4)$ $(z+1/4,y+1/4,x+1/4)$
48	G	$\cdot 2$	$(1/8,y,-y+1/4)$ $(-y+1/4,1/8,y)$ $(y,-y+1/4,1/8)$ $(7/8,-y,y+3/4)$ $(y+3/4,7/8,-y)$ $(-y,y+3/4,7/8)$	$(3/8,-y,-y+3/4)$ $(-y+3/4,3/8,-y)$ $(-y,-y+3/4,3/8)$ $(5/8,y,y+1/4)$ $(y+1/4,5/8,y)$ $(y,y+1/4,5/8)$	$(7/8,y+1/2,y+1/4)$ $(y+1/4,7/8,y+1/2)$ $(y+1/2,y+1/4,7/8)$ $(1/8,-y+1/2,-y+3/4)$ $(-y+3/4,1/8,-y+1/2)$ $(-y+1/2,-y+3/4,1/8)$	$(5/8,-y+1/2,y+3/4)$ $(y+3/4,5/8,-y+1/2)$ $(-y+1/2,y+3/4,5/8)$ $(3/8,y+1/2,-y+1/4)$ $(-y+1/4,3/8,y+1/2)$ $(y+1/2,-y+1/4,3/8)$
48	F	$2..$	$(x,0,1/4)$ $(0,1/4,x)$ $(x+3/4,1/2,1/4)$ $(-x,0,3/4)$ $(0,3/4,-x)$ $(-x+1/4,1/2,3/4)$	$(-x+1/2,0,3/4)$ $(0,3/4,-x+1/2)$ $(-x+1/4,0,1/4)$ $(x+1/2,0,1/4)$ $(0,1/4,x+1/2)$ $(x+3/4,0,3/4)$	$(1/4,x,0)$ $(3/4,x+1/4,0)$ $(0,1/4,-x+1/4)$ $(3/4,-x,0)$ $(1/4,-x+3/4,0)$ $(0,3/4,x+3/4)$	$(3/4,-x+1/2,0)$ $(3/4,-x+3/4,1/2)$ $(1/2,1/4,x+3/4)$ $(1/4,x+1/2,0)$ $(1/4,x+1/4,1/2)$ $(1/2,3/4,-x+1/4)$
32	E	$\cdot 3.$	(x,x,x) $(x+3/4,x+1/4,-x+1/4)$ $(-x,-x,-x)$ $(-x+1/4,-x+3/4,x+3/4)$	$(-x+1/2,-x,x+1/2)$ $(-x+3/4,-x+3/4,-x+3/4)$ $(x+1/2,x,-x+1/2)$ $(x+1/4,x+1/4,x+1/4)$	$(-x,x+1/2,-x+1/2)$ $(x+1/4,-x+1/4,x+3/4)$ $(x,-x+1/2,x+1/2)$ $(-x+3/4,x+3/4,-x+1/4)$	$(x+1/2,-x+1/2,-x)$ $(-x+1/4,x+3/4,x+1/4)$ $(-x+1/2,x+1/2,x)$ $(x+3/4,-x+1/4,-x+3/4)$

24	D	-4..	(3/8,0,1/4) (1/8,0,3/4) (1/4,3/8,0) (3/4,1/8,0) (0,1/4,3/8) (0,3/4,1/8) (3/4,5/8,0) (3/4,3/8,1/2) (1/8,1/2,1/4) (7/8,0,1/4) (0,1/4,7/8) (1/2,1/4,1/8)
24	C	2.2 2	(1/8,0,1/4) (3/8,0,3/4) (1/4,1/8,0) (3/4,3/8,0) (0,1/4,1/8) (0,3/4,3/8) (7/8,0,3/4) (5/8,0,1/4) (3/4,7/8,0) (1/4,5/8,0) (0,3/4,7/8) (0,1/4,5/8)
16	B	.32	(1/8,1/8,1/8) (3/8,7/8,5/8) (7/8,5/8,3/8) (5/8,3/8,7/8) (7/8,7/8,7/8) (5/8,1/8,3/8) (1/8,3/8,5/8) (3/8,5/8,1/8)
16	A	-.3.	(0,0,0) (1/2,0,1/2) (0,1/2,1/2) (1/2,1/2,0) (3/4,1/4,1/4) (3/4,3/4,3/4) (1/4,1/4,3/4) (1/4,3/4,1/4)

Table 2. Crystallographic information of S.G #220 [22].

Multiplicity	Wyckoff letter	Site symmetry	Coordinates			
			(0,0,0) + (1/2,1/2,1/2) +			
48	E	1	(x,y,z) (-x+1/2,-y,z+1/2) (-x,y+1/2,-z+1/2) (x+1/2,-y+1/2,-z) (z,x,y) (z+1/2,-x+1/2,-y) (-z+1/2,-x,y+1/2) (-z,x+1/2,-y+1/2) (y,z,x) (-y,z+1/2,-x+1/2) (y+1/2,-z+1/2,-x) (-y+1/2,-z,x+1/2) (y+1/4,x+1/4,z+1/4) (-y+1/4,-x+3/4,z+3/4) (y+3/4,-x+1/4,-z+3/4) (-y+3/4,x+3/4,-z+1/4) (x+1/4,z+1/4,y+1/4) (-x+3/4,z+3/4,-y+1/4) (-x+1/4,-z+3/4,y+3/4) (x+3/4,-z+1/4,-y+3/4) (z+1/4,y+1/4,x+1/4) (z+3/4,-y+1/4,-x+3/4) (-z+3/4,y+3/4,-x+1/4) (-z+1/4,-y+3/4,x+3/4)			
24	D	2..	(x,0,1/4) (-x+1/2,0,3/4) (1/4,x,0) (3/4,-x+1/2,0) (0,1/4,x) (0,3/4,-x+1/2) (1/4,x+1/4,1/2) (1/4,-x+3/4,0) (x+1/4,1/2,1/4) (-x+3/4,0,1/4) (1/2,1/4,x+1/4) (0,1/4,-x+3/4)			
16	C	.3.	(x,x,x) (-x+1/2,-x,x+1/2) (-x,x+1/2,-x+1/2) (x+1/2,-x+1/2,-x) (x+1/4,x+1/4,x+1/4) (-x+1/4,-x+3/4,x+3/4) (x+3/4,-x+1/4,-x+3/4) (-x+3/4,x+3/4,-x+1/4)			
12	B	-4..	(7/8,0,1/4) (5/8,0,3/4) (1/4,7/8,0) (3/4,5/8,0) (0,1/4,7/8) (0,3/4,5/8)			
12	A	-4..	(3/8,0,1/4) (1/8,0,3/4) (1/4,3/8,0) (3/4,1/8,0) (0,1/4,3/8) (0,3/4,1/8)			

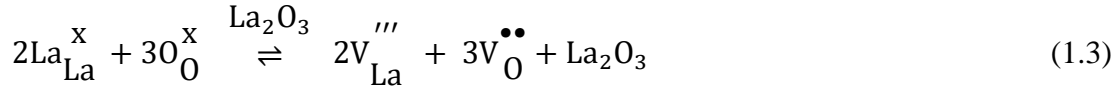
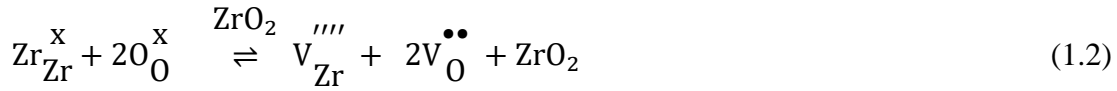
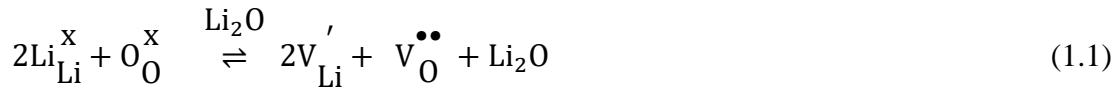
1.3. Defect chemistry in LLZO

Generally, point defects are categorized into two types i) intrinsic and ii) extrinsic in which a brief explanation of each is given in the following sections.

1.3.1. Intrinsic

1.3.1.1. Vacancies

Vacancy point defect is couple of cation and anion vacancy sites in a perfect crystal which is called Schottky defect (shown in **Figure 3**). The LLZO can have different cation and anion pairs of vacancies [16, 23]. Followings are the possible Schottky defect reactions for each pair:



Where V_{Li}' , V_{Zr}'''' , V_{La}'''' and $\text{V}_{\text{O}}^{\bullet\bullet}$ are Li^+ , Zr^{4+} , La^{3+} and O^{2-} vacancies in their crystal structures, respectively.

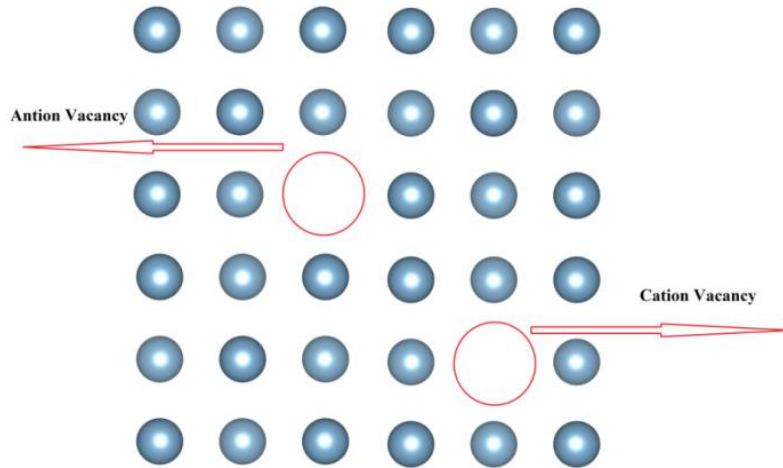


Figure 3. Representation of a pair of Schottky defect.

1.3.1.2. Interstitial

Another intrinsic defect is called Frenkel defect in which an atom leaves its position in the structure and occupies an interstitial site as demonstrated in **Figure 4** [16, 24]. The Frenkel defect reactions for ZrO_2 and La_2O_3 are written as below:





Where $\text{Li}_{\text{i}}^{\bullet}$, $\text{Zr}_{\text{i}}^{\bullet\bullet\bullet\bullet}$, $\text{V}_{\text{Zr}}^{\prime\prime\prime\prime}$, $\text{La}_{\text{i}}^{\bullet\bullet\bullet}$ and $\text{V}_{\text{La}}^{\prime\prime\prime}$ are Li^+ cation residing at the interstitial site, Li^+ vacancy, Zr^{4+} cation residing at the interstitial site, Zr^{4+} vacancy, La^{3+} cation residing at the interstitial site and La^{3+} vacancy, respectively.

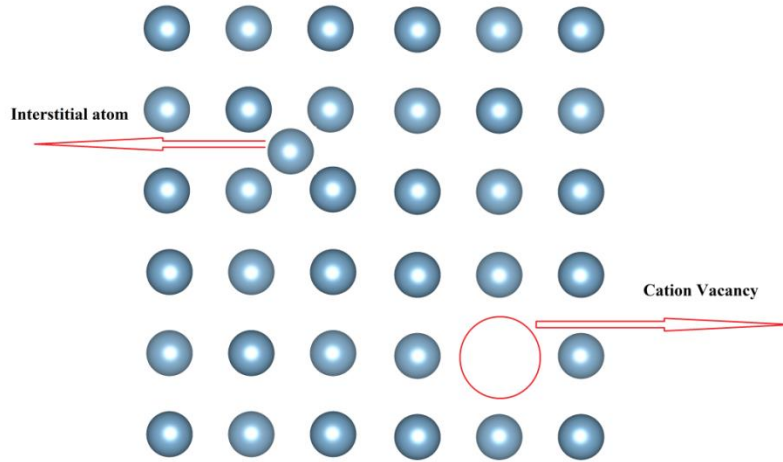
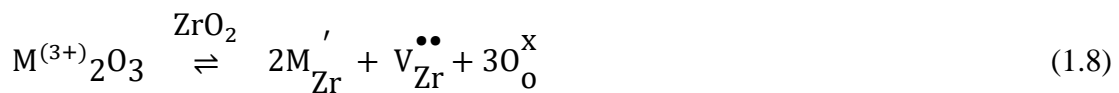
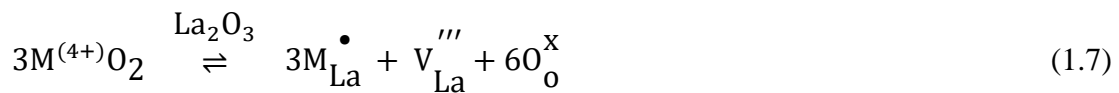


Figure 4. Representation of a pair of Frenkel defect

1.3.2. Extrinsic

1.3.2.1. Substitutional impurity

This is the most important type of defect in which the ionic conductivity of Li^+ is strongly dependant on it [16, 23, 25, 26]. Therefore, to further understand the Li^+ ion conduction in LLZO, we should dig into the possibilities of the formation of different vacancies. Hence, we will start doping La^{3+} , Zr^{4+} , and Li^+ sites with dopants having various valence charge (M^{n+}) with their corresponding Kröger - Vink reactions shown as below:





where M_{La}^{\bullet} , V_{La}''' , M_{Zr}' , M_{La}'' , M_{Zr}''' , $V_O^{\bullet\bullet}$ and O_O^x represent a M^{4+} ion residing at La^{3+} site with a charge of -1, a vacancy at a La^{3+} site with a charge of +3, an M^{3+} ion residing at Zr^{4+} site with a charge of +1, an M^{+} ion residing at La^{3+} site with a charge of +2, an M^{+} ion residing at Zr^{4+} site with a charge of +3, an oxygen vacancy at the O site with a charge of +3 and O occupying an O site with a neutral charge, respectively.

1.4. Impact of various dopants on LLZO

As it was mentioned before, vacancies play a vital role in increasing the ionic conductivity of LLZO by providing hopping sites for Li^{+} ions. Comparison of different polymorphs of LLZO (cubic and tetragonal), has revealed that the cubic phase has two times higher ionic conductivity than the tetragonal polymorph [27-30]. The reason arises from the fact that a minimum of 0.4–0.5 atoms per formula unit Li^{+} vacancy is required to obtain cubic phase [18, 25]. Hence, the phase transformation from tetragonal to cubic will only be possible by the incorporation of dopants to $Li_aM_xLa_bZr_cO_{12}$ with M being aliovalent cation and x being the concentration of the same which finally helps create vacancies in the structure. It is also possible to transform tetragonal to cubic phase without incorporating Al^{3+} or any other dopants. However, it demands careful tailoring of stoichiometry, higher temperatures, and does not increase ionic conductivity significantly [30-32]. Many factors impact the Li^{+} ion conductivity of cubic LLZO such as (a) charge carriers [23, 33, 34], (b) vacancy concentration [28], (c) coordination of Li^{+} ions [35-37], (d) dimensions of Li–O bonds [38], and (e) microstructure [27, 36, 39]. A brief explanation of some of the dopants are mentioned in the following sections.

1.4.1. Effect of Al^{3+}

In seek of dopant elements for stabilizing cubic phase, researchers found Al^{3+} , a dopant with low price and abundant availability, which demonstrated a good candidacy for raising the ionic conductivity of LLZO.

Generally, the incorporation of Al^{3+} has the following impacts on the LLZOs:

1. Stabilization and transformation of the tetragonal phase into cubic [37].
2. Blocking interstitial channels for Li^{+} diffusion [40].

3. Generating lithium vacancies for facilitating Li^+ movement [31].
4. Development of a Li–Al–O based amorphous phase which assists the grain boundaries diffusion of Li ions [41, 42].

Following defect reaction demonstrates the effect of Al^{3+} doping on Li vacancy formation:



Where $\text{Al}_{\text{Li}}^{\bullet\bullet}$, V_{Li}' and $\text{O}_{\text{O}}^{\times}$ are Al^{3+} ions sitting in a Li^+ position, Li^+ vacancy generated due to the charge imbalance and neutral oxygen, respectively.

It is clear from reaction (1.11) that two Al^{3+} can produce four Li^+ vacancies. However, this is valid for low concentrations of Al^{3+} . **Figure 5** demonstrates the polyhedral model of Al^{3+} doped LLZO. In this structure, Al^{3+} ions occupy 24d sites creating Li vacancies due to the charge imbalance.

The stable cubic phase of LLZO was first reported by the unintentional diffusion of Al^{3+} into LLZO [31, 41, 43-45]. In exploring the cause for this phenomenon, researchers investigated the mechanism in which the cubic phase is stabilized at room temperature by incorporation of Al^{3+} . For instance, Geiger et al. reported the unintentional formation of the cubic phase due to the reaction between alumina crucible and LLZO for the first time. This group suggested that Al^{3+} occupies Li^+ position and this may act as the stabilizing agent for the cubic phase in LLZO. This group suggested that Al^{3+} substitution with Li^+ generates Li^+ vacancies which then can lead to cubic phase stability. However, they did not mention the mechanism in which that Li^+ vacancy can lead to the achieving of the cubic phase [31].

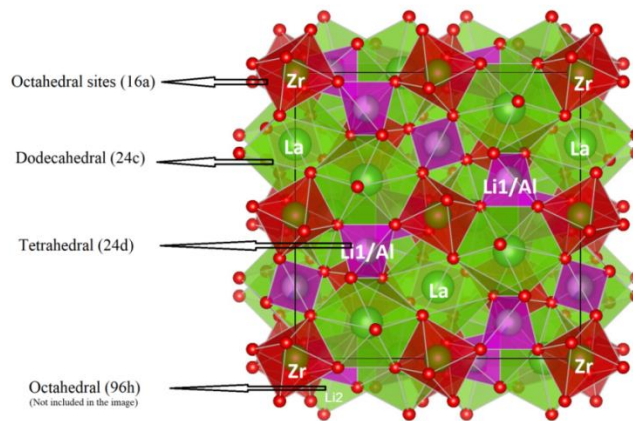


Figure 5. Polyhedral model of Al doped LLZO crystal structure.

Furthermore, Xia et al studied the impact of the crucible impurities on the Li ion transport properties of samples specifically sintered in alumina crucibles. The ionic conductivity reached by their group was relatively low ($4.48 \times 10^{-4} \text{ S.cm}^{-1}$) and this was

reported to be due to the extra Al^{3+} ions contamination from alumina crucibles, hence, leading to Li^+ loss during high-temperature sintering [44]. Another unintentional cubic LLZO was reported by Shimonishi et al in which they stated diffusion of Al^{3+} from alumina crucible into LLZO [46].

Further investigations revealed that adequate vacancies generated by Al^{3+} substitution, destroy well organized and ordered sublattice of Li^+ , and such a disorder, combined with the lattice relaxation favours the cubic phase. Additionally, the resultant vacancies open up the blocked Li^+ pathways for further enhancement of Li ion transport [45]. In another study, with the aid of neutron diffraction measurements, it was found that at lower temperature such as 4 K Li ion disorder exists which increases at room temperature and this increases the mobility of the Li^+ ions. These results approved the presence of Al^{3+} ions at 24d site [47, 48]. However, Duvel et al conducted an experiment using powder X-ray diffraction (PXRD) and Al^{3+} magic angle spinning nuclear magnetic resonance (MAS NMR) spectroscopy and demonstrated that there are three different sites that Al^{3+} can occupy, namely; La^{3+} , and Zr^{4+} [45]. Additionally, the presence of Al^{3+} at grain boundry has also been reported [49].

The tailoring of Al^{3+} concentration may lead to a pure cubic phase with a minor amount of impurity phases. It has been reported that optimum Al^{3+} concentration for the formation of the pure cubic phase with minor tetragonal impurities lies in the range of 0.19 to 0.4 pfu [27]. Additionally, when Al^{3+} concentration exceeds this value, the LaAlO_3 impurity phase starts to form. Overall, exceeding the optimum level of Al^{3+} concentration in LLZO will increase the risk of formation of impurity phases such as $\text{La}_2\text{Zr}_2\text{O}_7$, LaAlO_3 , $\gamma\text{-LiAlO}_2$, and $\text{La}_2\text{Li}_{0.5}\text{Al}_{0.5}\text{O}_4$ [7]. Additionally, it has been reported that Al^{3+} doping increases Li48g+96h/Li24d ratio as demonstrated [32, 44, 45].

The PXRD patterns of Al^{3+} doped LLZO are demonstrated in **Figure 6** [13]. It is obvious that increasing Al^{3+} content improves the crystallinity of the cubic phase and annihilates the tetragonal one.

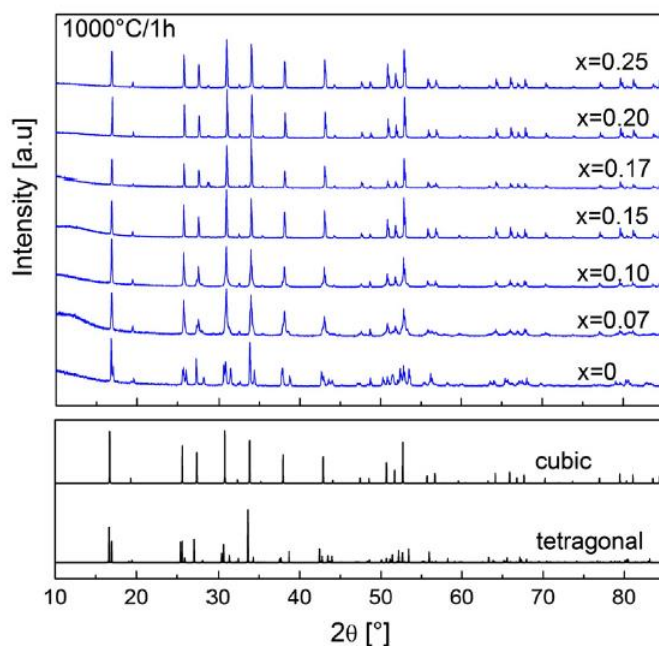


Figure 6. Impact of Al^{3+} content on crystallinity and purity of the cubic phase [13].

1.4.2. Effect of Ta^{5+} and Nb^{5+}

The problems arising from the creation of obstacles by Al^{3+} ions on Li^+ pathways have directed researchers to employ pentavalent doping strategy targeting Zr^{4+} site to introduce Li^+ vacancies [50]. To solve this problem, pentavalent cations such as Tantalum (Ta^{5+}) and Niobium (Nb^{5+}) have been introduced and have been shown to have a promising impact on improving ionic conductivity and stability of electrolyte in contact with electrodes. The general formula of this type of garnet has been proposed to be $\text{Li}_{7-x}\text{La}_3\text{M}_x\text{Zr}_{2-x}\text{O}_{12}$ with M being pentavalent cations of Ta^{5+} and Nb^{5+} [33, 51-61]. In this structure, La ions are coordinated in an 8-fold oxygen environment (24d), Ta/Nb/Zr ions are coordinated in an 6-fold oxygen environment (16a) and Li atoms reside at tetrahedral (24d) and octahedral sites (96h) [59]. The combination of Li^+ ions at tetrahedral and octahedral sites generate a network. In this three dimensionally connected network of Li ions, tetrahedral sites (24d) are connected to four other octahedral sites by sharing edges. Logéat et al. showed that Li^+ resides at all the octahedral sites and additionally at one-third of the tetrahedral sites [59]. Therefore, $[\text{La}_3\text{M}_x\text{Zr}_{2-x}\text{O}_{12}]^{5-}$ framework must accommodate five lithium cations using some combination of the three tetrahedral, six octahedral, and three trigonal prismatic sites [51] as illustrated in **Figure 7**.

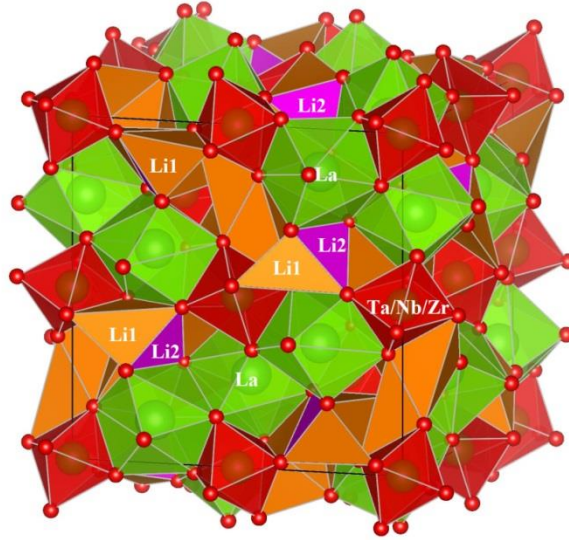


Figure 7. Polyhedral model of Ta⁵⁺/Nb⁵⁺ doped LLZO crystal structure.

Both cations can help LLZO phase transformation occur from tetragonal to cubic with a space group of Ia $\bar{3}$ d [55, 61]. Based on the general formula, Li_{7-y}La₃Zr_{2-y}M_yO₁₂, y needs to be as low as ~0.2 to obtain a cubic phase [25]. Despite Al³⁺, which replaces Li⁺ in LLZO crystal structure, Ta⁵⁺ and Nb⁵⁺ substitute for Zr⁴⁺ at octahedrally coordinated 16a position in which produces less Li⁺ vacancies (twice less in compared to Al³⁺ doping) [25, 51, 62]. When Zr⁴⁺ is replaced by Ta⁵⁺, Coulombic repulsion between Li⁺-Li⁺ ions is decreased by generation of Li⁺ vacancies. Therefore, the Ta⁵⁺-doped LLZO demonstrates enhanced conductivity than undoped LLZO [63].

Hence, the general defect reactions of Ta⁵⁺ and Nb⁵⁺ doped LLZO are written as below:



Where $\text{Ta}_{\text{Zr}}^{\bullet}$, $\text{Nb}_{\text{Zr}}^{\bullet}$, V_{Li}' and O_0^{\times} are Ta⁵⁺ sitting on a Zr⁴⁺ position, Nb⁵⁺ sitting on a Zr⁴⁺ position, Li⁺ vacancy generated due to the charge imbalance and neutral oxygen, respectively. As it was mentioned earlier, Ta⁵⁺ cations act as the gate opener for Li⁺ ions. In this regard, Shin et al. showed that doping Al-LLZO with Ta⁵⁺ causes the Li ions to change their site from 24d to 96h site opening up the pathways of Li⁺ ions to diffuse [28].

Figure 8 and **Figure 9** represents the effect of different amounts of Ta^{5+} and Nb^{5+} dopant on the crystallization of the LLZO cubic phase, respectively [55, 59]. As is seen from the XRD patterns for both cases, increasing dopant content increases the crystallinity of the cubic phase and, thereafter, ionic conductivity.

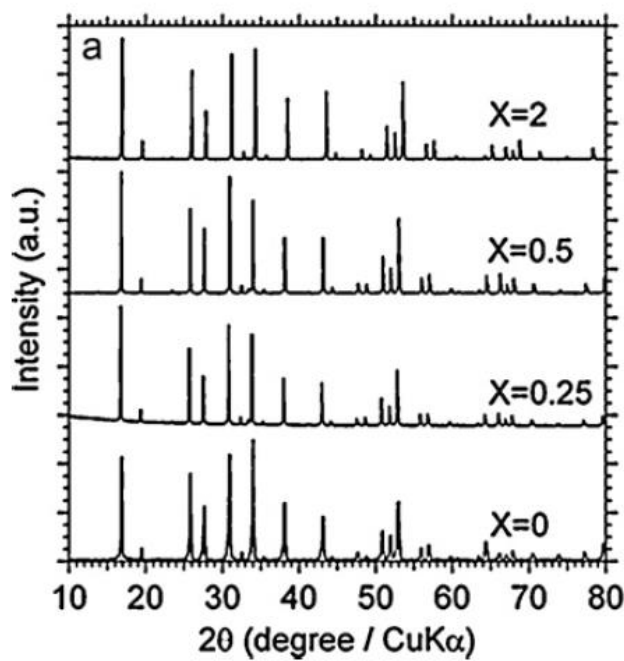


Figure 8. XRD patterns of LLZO doped with different amounts Nb^{5+} [55].

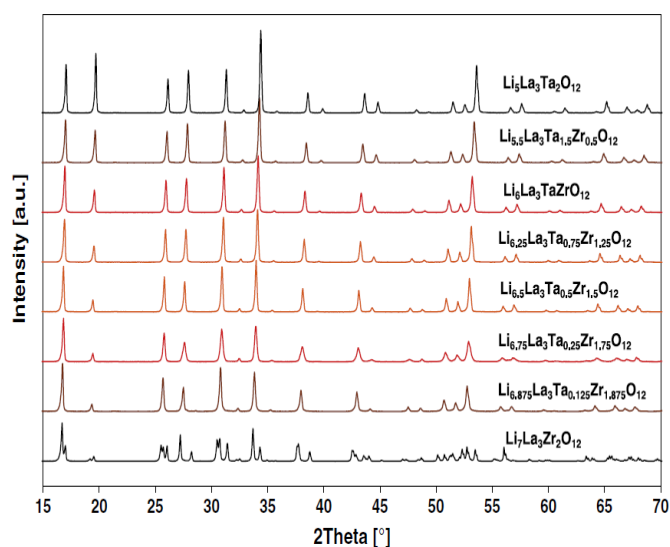


Figure 9. XRD patterns of LLZO doped with different amounts Ta^{5+} [59].

1.4.3. Effect of Ge⁴⁺

Ge⁴⁺ stands in the fourth group of the periodic table of the element which has four valence electrons on its outer shell. In the LLZO structure, Ge⁴⁺ can substitute for Li⁺ or La³⁺ sites which might be favorable for the ionic conduction. As it was observed in other doped LLZOs, the cubic phase is desirable since it can enhance the ionic conductivity (7.63×10^{-4} S.cm⁻¹ at 298 K) dramatically [64]. Here also, the cubic phase can be obtained by incorporation of 1 wt% of Ge⁴⁺. However, cubic and tetragonal polymorphs coexist when the concentration of the dopant ions exceeds this value [65].



where $\text{Zr}_{\text{La}}^{\bullet}$, $V_{\text{La}}^{\prime\prime\prime}$ and O_0^{X} represent a Zr⁴⁺ occupying a La³⁺ site with an overall charge of -1, a La³⁺ vacancy an overall charge of +3, and a neutral oxygen atom, respectively.

The structure of Ge⁴⁺ doped LLZO is made of LaO₈ and ZrO₆ polyhedrals by sharing edges, which is illustrated in **Figure 10**. In this **Figure**, the greens show LaO₈ dodecahedra substituted partially by Ge⁴⁺ and the blues show the ZrO₆ octahedra. Huang et al. reported that if Ge⁴⁺ ion resides at the La³⁺ site, the polyhedron is disconnected. Four oxygen ions are connected to the neighboring LaO₈ dodecahedral, while four oxygen atoms surround the Ge⁴⁺ ions. Since the ionic radius of Ge⁴⁺ ions is smaller than that of La³⁺ ions, substitution of Ge would cause distortion and contraction of lattice [65]. In their phase analysis (**Figure 11**), they showed that at lower doping contents (0.25wt% to 1wt %), the structure was found to be cubic phase. However, at higher Ge contents, 2 wt %, an impurity phase started to appear.

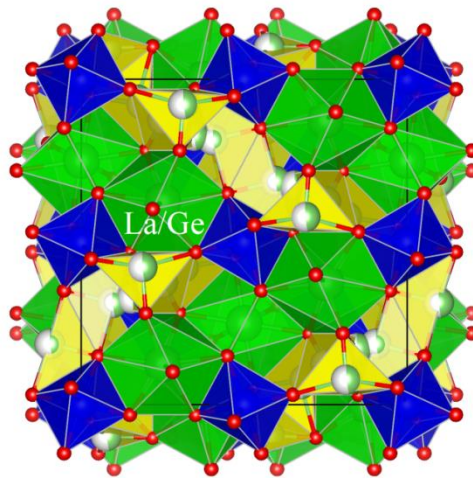


Figure 10. Polyhedral model of Ge doped LLZO crystal structure.

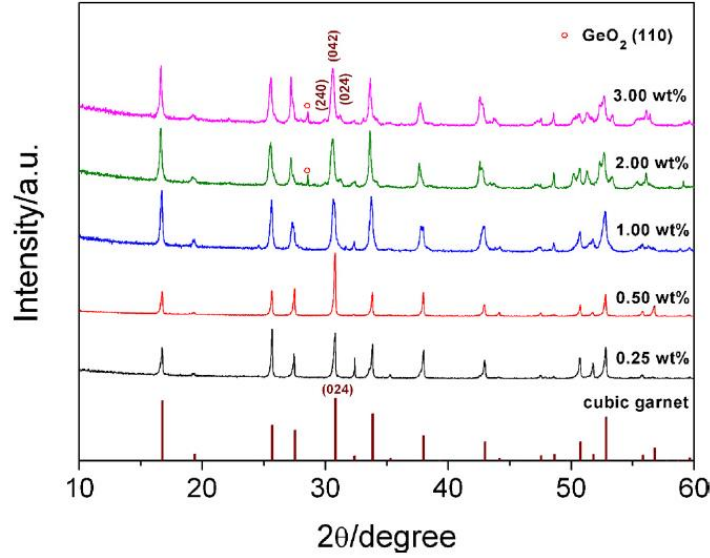


Figure 11. XRD patterns of LLZO doped with different amounts of Ge⁴⁺ [65].

In another work conducted by Peng et al, synthesis of garnet-related structure of Li_{5+x}La₃Ge_xNb_{2-x}O₁₂ by direct use of metallic Ge was investigated and their Li ion transport properties and stability against Li-metal were investigated. The XRD results of Li_{5+x}La₃Ge_xNb_{2-x}O₁₂ (x = 0.25-1) samples approved the presence of the cubic phase. In their research, Ge⁴⁺ substituted for Nb⁵⁺ and the total conductivity of Li_{5.75}La₃Ge_{0.75}Nb_{1.25}O₁₂ was observed to be 1.2×10⁻⁴ S.cm⁻¹ [66].

1.4.4. Effect of Ga³⁺

Further interest in employing different supervalent dopants has led researchers to examine the effect of Ga³⁺ on LLZOs. In this regard, many researchers have tested different concentrations and, therefore, the impact of Ga³⁺ on the structure and ionic conductivity of LLZO [67-82].

Based on their research, Ga³⁺ has been found to be successful in converting the tetragonal phase into cubic [70]. Same as all other dopants, Ga³⁺ itself can induce vacancies followed by disorder in the structure of LLZO. To further understand the mechanism in which Ga³⁺ produces defects, its defect reaction is proposed. The defect reaction of Ga³⁺ doped LLZO is written as below:



Where $\text{Ga}_{\text{Li}}^{\bullet\bullet}$, V_{Li}' and $\text{O}_{\text{O}}^{\text{x}}$ are Ga^{3+} ions sitting in Li^+ position, Li^+ vacancy generated due to the charge imbalance and neutral oxygen, respectively.

According to (1.16), by incorporation of one Ga^{3+} into the structure of LLZO, two Li vacancies are generated. The Ga^{3+} doped LLZO has shown to have higher ionic conductivity in comparison to other doped LLZOs. The cause for such an enhancement in ionic conductivity by Ga^{3+} Addition is still not fully understood. However, Rettenwander et al. in their second study [79] using ^{71}Ga MAS NMR spectra showed that Ga^{3+} occupies both 24d and 96h sites which creates new paths for Li^+ ions to move easier. This research group could not observe this behavior in their earlier study [78] and this invisibility at the lower magnetic field was attributed to the large second-order quadrupolar broadening which influences ^{71}Ga NMR spectra and makes it difficult to distinguish peaks. Further studies revealed that Ga^{3+} doped LLZO has an acentric cubic SG $\text{I}\bar{4}3\text{d}$ (no. 220) which is an unusual symmetry in comparison with other Li-stuffed garnet groups that demonstrate centric cubic SG $\text{Ia}\bar{3}\text{d}$ (no.230) [81].

Further investigations by Rettenwander et al. revealed the detailed crystal structure of cubic Ga^{3+} doped LLZO with a space group of $\text{Ia}\bar{3}\text{d}$ (no.230) and $\text{I}\bar{4}3\text{d}$ (no.220) (shown in **Figure 12 a,b,c, and d**). In Figure 12a, the blue and green geometries belong to La^{3+} and Zr^{4+} sites at dodecahedral and octahedral positions. Additionally, Li^+ can be found in three different sites such as tetrahedral 24d, octahedral 48g and tetrahedral 96h. The pathway concerned with Li ion diffusion is represented at (b). **Figure 12c** demonstrates the crystal structure of cubic LLZO with space group SG $\text{I}\bar{4}3\text{d}$ (no. 220) leads to different site preferences. In this structure, La^{3+} occupies dodecahedra (blue 24d), Zr^{4+} occupies octahedra (green 16c) sites, respectively. Li^+ ions reside at three different positions; namely two 4-fold sites at 12a and 12b positions shown red and orange colors and 6-fold sites positioned at 48g shown in yellow. The diffusion pathway concerned with Li is demonstrated at (d) [80]. Rettenwander et al. also reported that Li^+ conductivity of Ga-LLZO is two times higher than Al-LLZO [8, 27, 69].

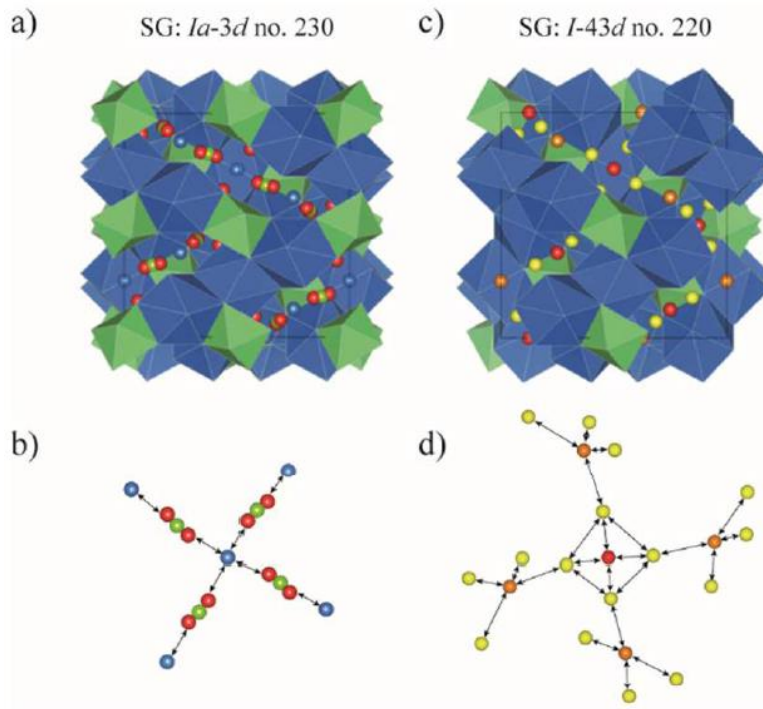


Figure 12. representation a) Centric cubic structure with space group of $Ia\bar{3}d$ (no.230). b) Centric cubic structure with space group of $I\bar{4}3d$ (no.220). c) Li ion pathway of $Ia\bar{3}d$ (no.230). d) Li ion pathway of $I\bar{4}3d$ (no.230) [80].

Increasing in Ga^{3+} concentration does not vary the lattice parameters and and also it does not induce any change to the site preference of cations dramatically. The only change is associated with the site occupancy of Li which is encouraged to occupy $24d$ sites. **Figure 13** demonstrates the effect of Ga content on the XRD patterns of LLZO. It is obvious that increasing Ga content improves the crystallinity of this phase [82].

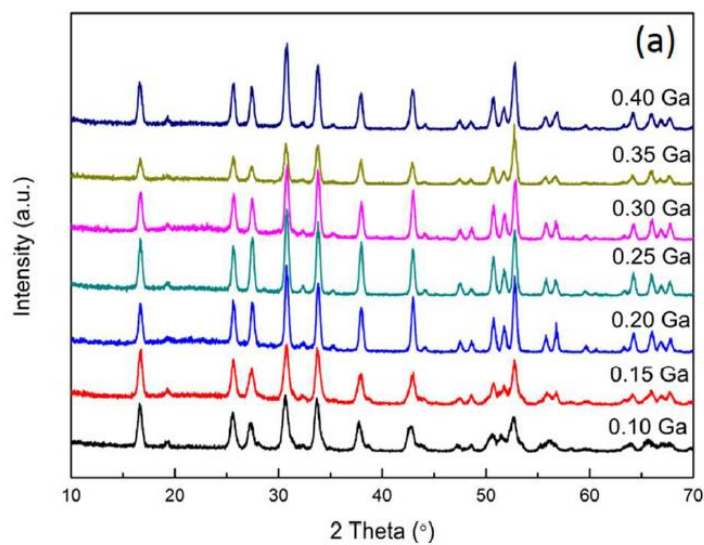


Figure 13. XRD patterns of Ga^{3+} doped LLZO with different amounts of Ga^{3+} [82].

1.4.5. Effect of Sb^{5+}

The Sb^{5+} is a pentavalent element and has proved to have the same behaviour as Nb^{5+} and Ta^{5+} when doped to LLZO. The **Figure 14** demonstrates the crystal structure of Sb^{5+} doped LLZO.

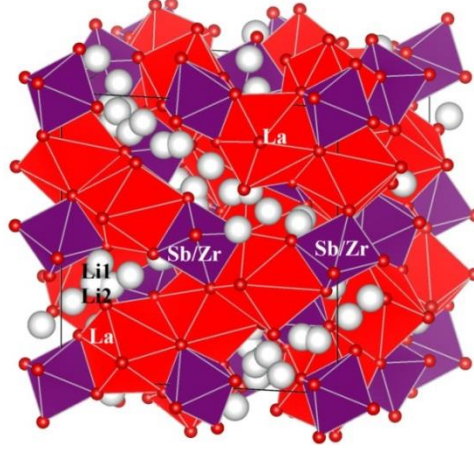
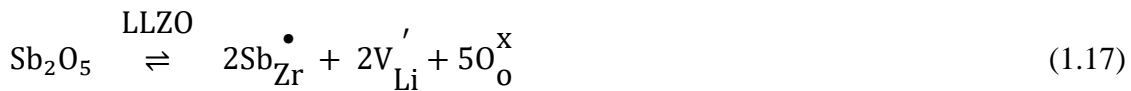


Figure 14. Polyhedral model of Sb doped LLZO crystal structure.

In this regard, Ramakumar et al. successfully synthesized the Sb^{5+} -substituted Li-garnets $\text{Li}_{7-x}\text{La}_3\text{Zr}_{2-x}\text{Sb}_x\text{O}_{12}$ ($x = 0.2, 0.4, 0.6, 0.8$ and 1.0) using a conventional solid-state method [21]. Based on the literature, Sb^{5+} partially substitutes for Zr^{4+} and stabilizes the cubic phase at room temperature [21, 83, 84]. During the incorporation of Sb^{5+} into LLZO, an increase in ionic conductivity ($7.7 \times 10^{-4} \text{ S.cm}^{-1}$) has been observed. This increase in ionic conductivity is attributed to an increase in Li^+ ions occupying tetrahedral sites and a decrease in Li^+ ions occupying octahedral sites [21]. Another work conducted by Cao et al., using codoping of Sb^{5+} and Ba^{2+} , resulted in an improvement in grain boundary conductivity through the formation of a thin film on grain boundary while the bulk conductivity increased due to the increased occupancy of the Li2 site [84].

The following is the defect reaction of Sb^{5+} doped LLZO:



Where $\text{Sb}_{\text{Zr}}^{\bullet}$, V_{Li}' and $\text{O}_{\text{O}}^{\times}$ are Sb^{5+} sitting on a Zr^{4+} position, Li^+ vacancy generated due to the charge imbalance and neutral oxygen, respectively.

Yang et al investigated co-doping of Al^{3+} and Sb^{5+} into LLZO claiming that co-substitution of Sb^{5+} for Zr^{4+} and Al^{3+} for Li^+ facilitates the sintering of modified LLZO and enhances the

contact between grains. The $\text{Li}_{6.775}\text{Al}_{0.05}\text{La}_3\text{Zr}_{1.925}\text{Sb}_{0.075}\text{O}_{12}$ sintered at $1170\text{ }^\circ\text{C}$ exhibited an enhanced total Li^+ conductivity of $4.10 \times 10^{-4}\text{ S.cm}^{-1}$ at room temperature [83].

Figure 15 represents the effect of Sb^{5+} concentration on the crystallization of LLZO. As is seen from the Figure, some impurity phases Li_2ZrO_3 and Li_3SbO_4 have been detected in some compositions [21].

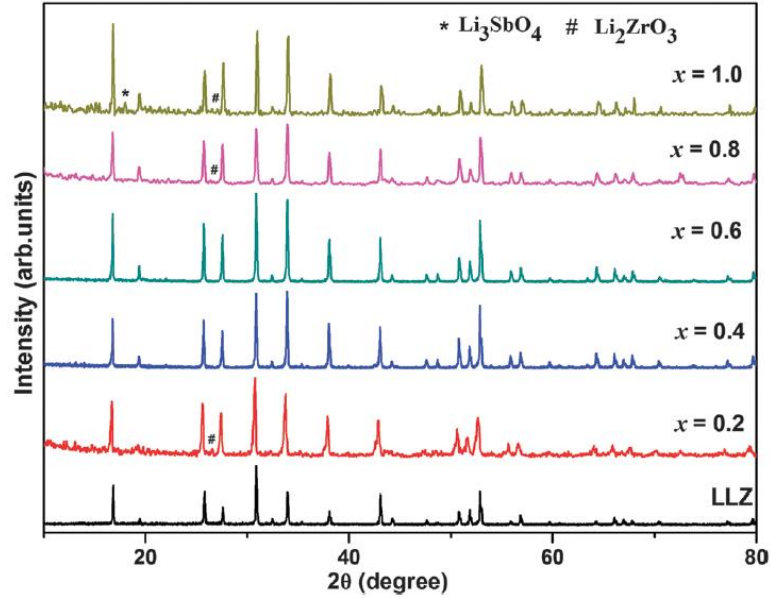


Figure 15. XRD patterns of LLZO doped with different amounts Sb^{5+} [21].

1.4.6. Effect of Fe^{3+}

As already discussed in previous sections, LLZO can transform into two different polymorphs: a tetragonal phase (space group (SG) $I41/acd$), and cubic phase (centric SG $Ia\bar{3}d$ and the acentric SG $I\bar{4}3d$), [20, 81]. Based on the literature, Fe^{3+} can stabilize LLZO into cubic form but with an acentric SG $I\bar{4}3d$ (No.220).

Following is the defect reaction of Fe^{3+} doped LLZO:



Where $\text{Fe}_{\text{Li}}^{\bullet\bullet}$, V_{Li}' and $\text{O}_{\text{O}}^{\times}$ are Fe^{3+} ions sitting in Li^+ position, Li^+ vacancy generated due to the charge imbalance and neutral oxygen, respectively.

The acentric SG $I\bar{4}3d$ (No.220) crystal structure has also been reported for Ga^{3+} -stabilized LLZO and is different from those of other members of the Li-stuffed garnet group which had SG $Ia\bar{3}d$ (No. 230) [20]. In the case of Ga^{3+} doped LLZO, the formation of acentric SG $I\bar{4}3d$ (No.220) crystal structure is attributed to the site preference of Ga^{3+} , which causes the splitting of the 24d position of SG $Ia\bar{3}d$ into two different sites, namely, Li1 (12a) and Li2 (12b). The same phenomenon happens for Fe^{3+} doped LLZO. The reason for such a phase transformation in Fe^{3+} doped LLZO is caused by the site preference of Fe^{3+} for the tetrahedral Li1 (12a) position. In this regard, Wagner et al showed that substitution of Li^+ with Fe^{3+} in LLZO induces a reduction in symmetry to SG $I\bar{4}3d$. Thereby, Fe^{3+} strongly prefers the Li1 (12a) site and its crystal structure is shown in **Figure 16** [1]. The comparison of Li^+ ion conductivities of LLZO polymorphs revealed that acentric polymorph (SG $I\bar{4}3d$) owns the higher ionic conductivity ($1.3 \times 10^{-3} \text{ S.cm}^{-1}$) [3] which is one order of magnitude higher than that of the conventional centric cubic garnet ($10^{-4} \text{ S.cm}^{-1}$) phase (SG $Ia\bar{3}d$) and three order of magnitude higher than that of tetragonal phase (SG $I41/acd$) ($10^{-6} \text{ S.cm}^{-1}$).

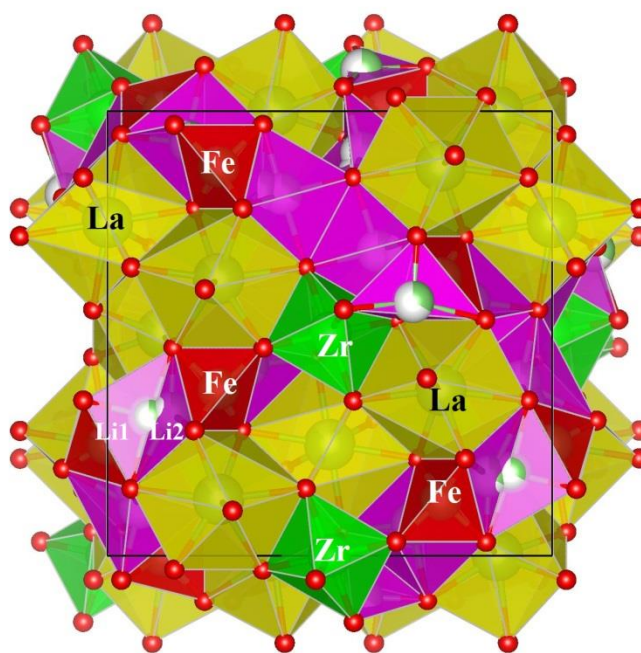


Figure 16. Polyhedral model of Fe^{3+} doped LLZO crystal structure with acentric SG $I\bar{4}3d$ (No.220)

Shown in **Figure 17**, increasing the Fe content, increase the crystallinity of the compound to an extent and then above $x=0.25$, minor impurity peaks appear. The peak at 21.63° , is specific to SG $I\bar{4}3d$ demonstrating that by incorporating Fe into the LLZO, the compound crystallize at $I\bar{4}3d$ symmetry.

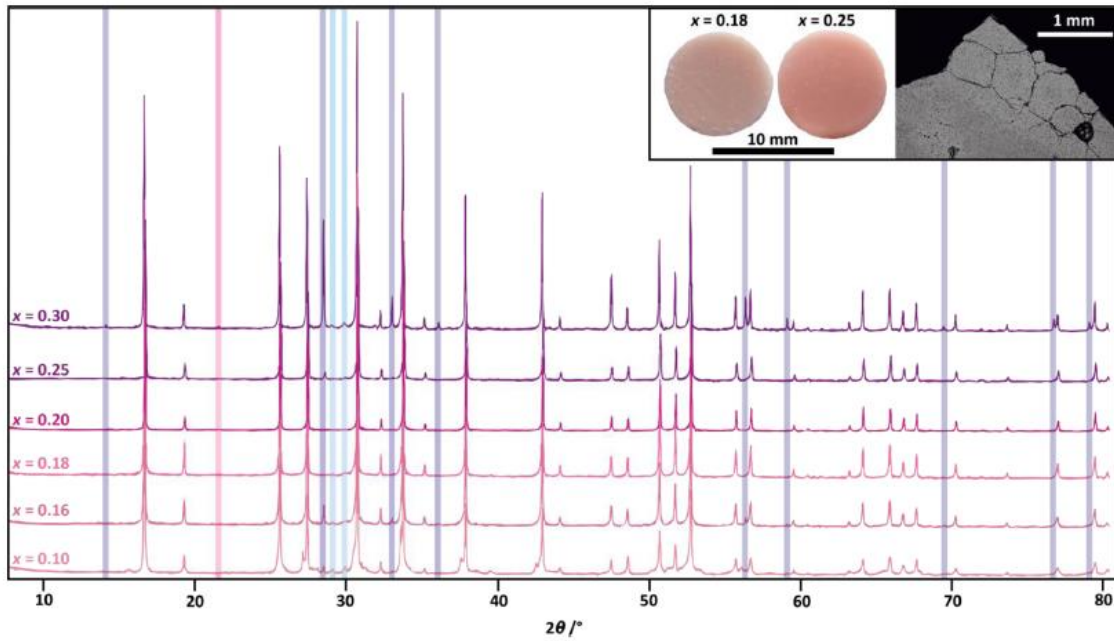


Figure 17. XRD patterns of LLZO doped with different amounts Fe^{3+} [20].

1.5. Solid state NMR theory

The solid-state NMR spectroscopy is usually conducted for ceramic materials in parallel with XRD and Neutron Diffraction (ND) to evaluate the validity of the latter ones. Therefore, it is a powerful tool to understand the structure of the materials especially the site preference of dopant ions. This method is also applicable for the materials without long-range order such as glasses and polymers.

The mechanism in which it operates is dependent on the interaction of subatomic particles with each other and also their interaction with the magnetic field generated by the NMR device. Therefore, followings are the possible interactions between subatomic particles and magnetic field:

1. Nucleus spin- magnetic field interaction: Zeeman interaction
2. Nuclei- Nuclei interaction: Direct Dipole-Dipole interaction
3. Nucleus spin- Electron-Nucleus spin: J-Coupling
4. Nuclei- Electron-Magnetic field: Chemical Shift
5. Nucleus-Electron: Quadrupole interaction

Among the above interaction, quadrupole interaction is the only one that involves the electric field around the nucleus. The other interactions are the ones engaged with magnetic field. In quantum physics, the subatomic interactions are shown using Hamiltonian operators. Hamiltonian is an operator which can include all of the abovementioned terms. Using this operator, one can understand the behavior of nuclei in the presence of a magnetic field and all

the other interactions. Each of the above terms can be written as a Hamiltonian function in quantum mechanics as below:

1.5.1. Zeeman Interaction

This interaction occurs between the Nucleus spin and the magnetic field. Equation (1.19) displays the mathematical terms regarding this interaction.

$$H^Z = -\gamma_j \vec{I}_j \cdot \vec{B} = -\gamma_j [I_{jx} \quad I_{jy} \quad I_{jz}] \begin{bmatrix} B_x \\ B_y \\ B_z \end{bmatrix} \quad (1.19)$$

Where γ_j is the magnetogyric ratio which is specific to the nuclei of an element, \vec{I}_j is the angular momentum and B is the magnetic field. The Zeeman interaction is rather stronger among interactions in the subatomic scale [85-88]. Therefore, better NMR resolution is dependent on the strength of the applied magnetic field. The stronger the magnetic field, the higher the resolution (signal to noise ratio) of the NMR spectrum for solid materials.

1.5.2. Direct Dipole-Dipole interaction

This interaction is generated between Nuclei. Equation (1.20) represents the mathematical terms regarding this interaction.

$$H_{jk}^{DD} = \vec{I}_j \cdot \vec{D}_{jk} \cdot \vec{I}_k = [I_{jx} \quad I_{jy} \quad I_{jz}] \begin{bmatrix} D_{xx} & D_{xy} & D_{xz} \\ D_{yx} & D_{yy} & D_{yz} \\ D_{zx} & D_{zy} & D_{zz} \end{bmatrix} \begin{bmatrix} I_{kx} \\ I_{ky} \\ I_{kz} \end{bmatrix} \quad (1.20)$$

Where D is Dipole-dipole tensor, which couples angular momentum of \vec{I}_j to the angular momentum of \vec{I}_k . In comparison to Zeeman interaction, this one is rather weaker [85-88].

1.5.3. J-coupling

This interaction involves Nucleus spin – Electron– Nucleus spin. Equation (1.21) demonstrates the mathematical terms regarding this interaction:

$$H_{jk}^J = \vec{I}_j \cdot \vec{J}_{jk} \cdot \vec{I}_k = [I_{jx} \quad I_{jy} \quad I_{jz}] \begin{bmatrix} I_{xx} & I_{xy} & I_{xz} \\ I_{yx} & I_{yy} & I_{yz} \\ I_{zx} & I_{zy} & I_{zz} \end{bmatrix} \begin{bmatrix} I_{kx} \\ I_{ky} \\ I_{kz} \end{bmatrix} \quad (1.21)$$

Where \vec{I}_{jk} is J coupling tensor, which couples angular momentum of \vec{I}_j to the angular momentum of \vec{I}_k . In compared to the other interactions, this is the weakest one [85-88].

1.5.4. Chemical Shift

This interaction is produced between Nuclei – Electron – Magnetic field and Equation (1.22) represents the mathematical terms regarding this interaction.

$$H_j^{CS} = -\gamma_j \vec{I}_j \cdot \vec{\delta}_j \cdot \vec{B} = [I_{jx} \quad I_{jy} \quad I_{jz}] \begin{bmatrix} \delta_{xx} & \delta_{xy} & \delta_{xz} \\ \delta_{yx} & \delta_{yy} & \delta_{yz} \\ \delta_{zx} & \delta_{zy} & \delta_{zz} \end{bmatrix} \begin{bmatrix} B_x \\ B_y \\ B_z \end{bmatrix} = \omega_{cs} \vec{I}_z \quad (1.22)$$

Where $\vec{\delta}_j$ is shielding tensor, which couples the spin angular momentum \vec{I}_j to the magnetic field \vec{B} and ω_{cs} is chemical shift frequency [85-88]. This interaction is the most studied one among the researchers for LLZO electrolytes. Applied magnetic field circulates the electrons in atoms which, in turn, induces a secondary magnetic field where it might not necessarily be in the same direction with the applied field to the nuclear spin. Therefore, to relate these two vectors to each other, shielding tensor is used. Following equation is representing the relation between the applied magnetic field and the induced one:

$$B_j^{induced} = \vec{\delta}_j \cdot B^{applied} \quad (1.23)$$

1.5.5. Quadrupole interaction

This interaction is established between the Nucleus and Electron and following Equations represents the mathematical terms regarding this interaction.

$$H_j^Q = \frac{eQ}{2I(2I-1)\hbar} [V_{zz} (3\hat{I}_z^2 - \vec{I} \cdot \vec{I})] \quad (1.24)$$

$$C_Q = \frac{eQV_{zz}}{\hbar} \quad (1.25)$$

$$\eta_Q = \frac{V_{xx} - V_{yy}}{V_{zz}} \quad (1.26)$$

Where e is the electronic charge, Q is the isotope-specific nuclear quadrupolar moment, V is a second-rank (3×3) symmetric tensor with nine terms corresponding to the electric field gradient at the nucleus C_Q is the magnitude of quadrupolar coupling constant and η_Q is the asymmetry parameter which is a number $0 \leq \eta_Q \leq 1$ [85-88].

The quadrupolar nuclei are prevalent in NMR; ~25% of NMR-active nuclei are spin $I = 1/2$ and ~75% are quadrupolar. In atoms with a nucleus larger than $I > 1/2$, electric multipole

moments are generated. These moments are produced due to the non-uniform charge distributions within the nuclei. The lack of non-uniformity in charge distributions is called quadrupolar moment (Q). The quadrupolar interaction is the strongest interaction among the other interactions mentioned above which usually induces satellite transitions to the spectrum and broadens the peaks.

1.5.6. ^7Li and ^6Li spectra of LLZO

Solid-state NMR has been used in recent decades to understand the local chemical environment of ceramic materials. By the emergence of solid electrolytes, specifically, LLZO materials, this device has turned into a powerful tool in order to have a better understanding of the LLZO structure. The NMR spectroscopy advancement has rocketed in recent years which have enabled researchers to have better resolution of spectrum for their materials. For instance, nowadays, NMR devices can reach to a magnetic field as high as 22 T along with Magic Angle Spinning (MAS) rate of 100 KHz. These capabilities in such an NMR spectrometer produce very sharp peaks for ions in their relevant spectra. Following spectra (**Figure 18** and **19**) demonstrate the advancement of Li^+ ion detection using a) old and b) new NMR machines [79].

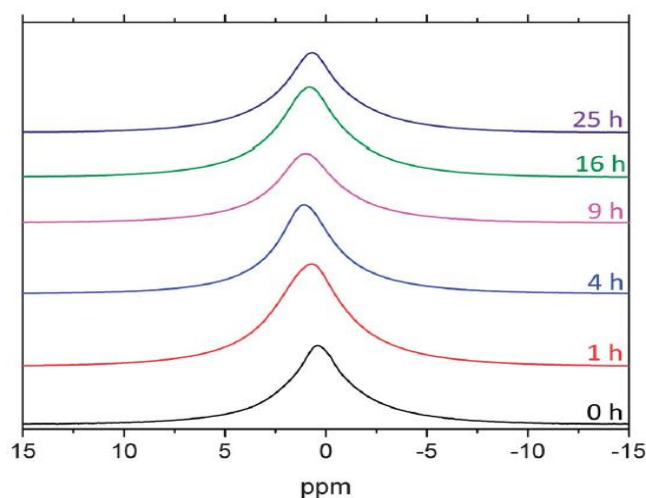


Figure 18. ^7Li NMR spectra recorded by an old NMR device (10T)

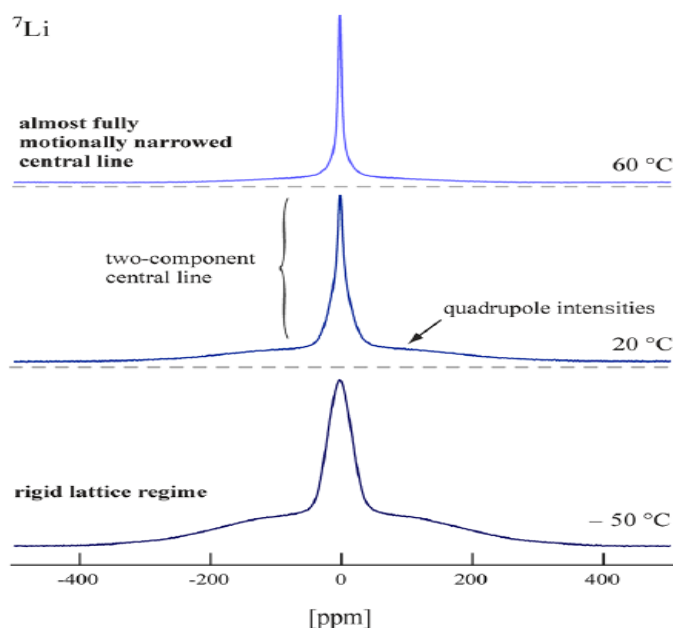


Figure 19. ${}^7\text{Li}$ NMR spectra recored by a new NMR device (21T) [79].

The ${}^7\text{Li}$ ($I = 3/2$) and ${}^6\text{Li}$ ($I = 1$) with the natural abundance of 92.58% 7.42%, respectively [89], are quadrupolar and highly dependent on the interaction of surrounding electric field gradient and their relevant quadrupolar moment (-4×10^{-2} and -8×10^{-4} , respectively) [79]. Therefore, such nuclei have lower symmetry and give rise to a central line flanked with two satellite transitions [90]. Since the nuclei are quadrupolar, the NMR spectrum of ${}^7\text{Li}$ is expected to appear broader due to the rapid relaxation. The broadening of the line is also a sign of the presence of asymmetry. This broadening arises from a larger distribution and diversity of chemical environments (Li occupying different sites) with a higher rate of disorder surrounding the Li cations [9]. Additionally, the shape of the central transitions provides a sense of the distribution of Li jump rates and Li migration pathways in garnets [90]. There is a strong correlation between Li solid-state NMR chemical shifts and the local environment of the garnet structure. This capability in NMR can provide us the information about the coordination number of Li and also the number of sites that Li occupies in the structure.

1.5.7. ${}^{27}\text{Al}$, ${}^{139}\text{La}$, ${}^{71}\text{Ga}$, ${}^{17}\text{O}$, and ${}^{45}\text{Sc}$ spectra

As mentioned in previous sections, LLZO research is falling into a trend of incorporating supervalent dopant ions into the structure to improve the ionic conductivity. Intense solid-state NMR studies have been performed on Al^{3+} doped LLZO to understand the local chemistry and its relevant coordination environment. As an example, Hubaud et al. [48] studied the chemical environment of Al^{3+} doped LLZO using ${}^{27}\text{Al}$ MAS NMR spectra with an 11.7 Tesla superconducting magnet in a 4 mm MAS probe which had 14 kHz spinning frequency. They set the MAS NMR measurements to have a pulse duration of 1.5 ms along

with a delay time of 1 s after each pulse. **Figure 20** demonstrates ^{27}Al NMR spectra of LLZO the samples sintered at different time durations [48].

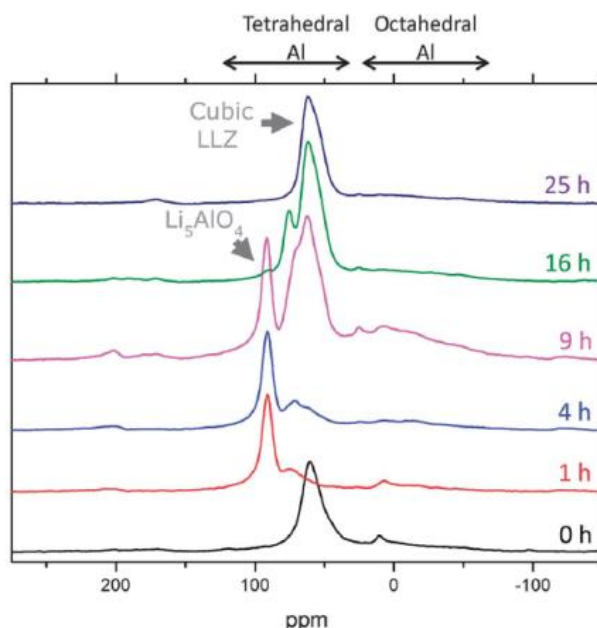


Figure 20. ^{27}Al MAS NMR spectra of Al^{3+} doped LLZO [48].

Same as ^{27}Al , NMR spectra and the chemical environment of other dopants such as ^{139}La , ^{71}Ga and ^{45}Sc have been investigated. In this regard, Spencer et al. obtained NMR spectrum of ^{139}La (shown in **Figure 21**) for $\text{LaLi}_{0.5}\text{Fe}_{0.2}\text{O}_{2.09}$ garnet at 21.1 T and they reported that in this structure, La^{3+} can be found in two different environments, namely La1 and La2. Using DMFit software, they calculated quadrupolar coupling constants and asymmetry parameters for these two environments (La2 has $C_Q = 56\text{MHz}$ and $\eta = 0.05$, La1 has $C_Q = 29\text{MHz}$ and $\eta = 0.6$) [91].

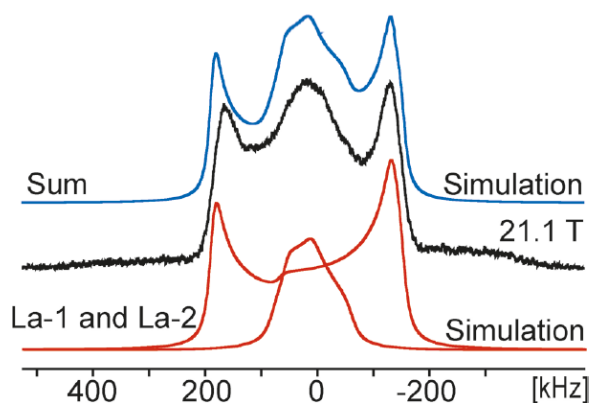


Figure 21. Experimental and simulated ^{139}La MAS NMR spectra of $\text{LaLi}_{0.5}\text{Fe}_{0.2}\text{O}_{2.09}$ structure [91].

In the case of ^{71}Ga , Rettenwander et al. recorded MAS NMR spectra of Ga doped LLZO (shown in **Figure 22**) at 21.1 T and they revealed two ^{71}Ga NMR resonances, corresponding to Ga occupying both the 24d (243 ppm) and 96h sites (193 ppm) [79]. Furthermore, they calculated C_Q for both 24d and 96h sites to be 3.9 and 11.4, respectively.

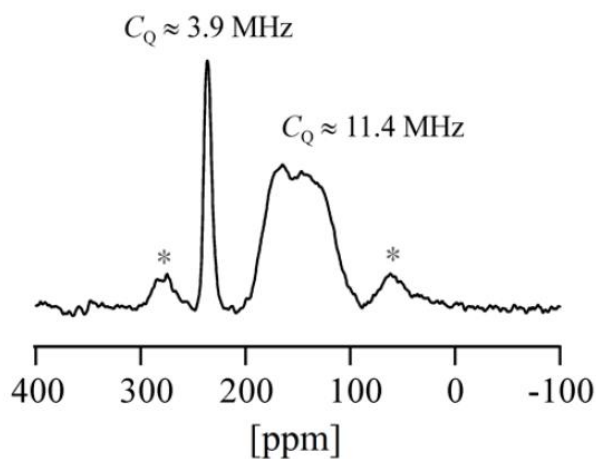


Figure 22. ^{71}Ga MAS NMR spectra of Ga^{3+} doped LLZO

In another study conducted by Buannic et al., ^{71}Ga and ^{45}Sc spectra of $\text{Sc}^{3+}/\text{Ga}^{3+}$ doped LLZO were obtained and they observed a signal at 140 ppm corresponding to 16a site and this approved the partial substitution of Sc^{3+} in Zr^{4+} site [9].

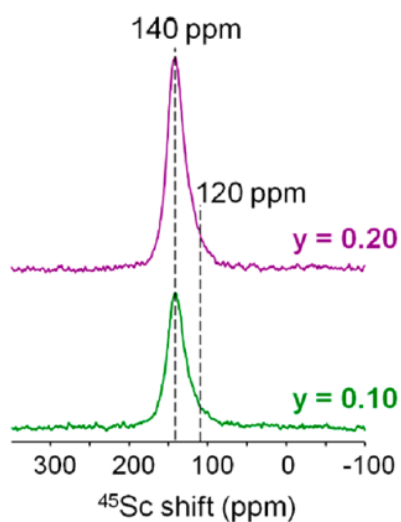


Figure 23. ^{45}Sc MAS NMR spectra of $\text{Sc}^{3+}/\text{Ga}^{3+}$ doped LLZO [9].

Finally, ^{17}O spectrum of the $\text{Ga}^{3+}/\text{Al}^{3+}$ doped LLZO (shown in **Figure 24**) was acquired by Karasulu et al. group. In ^{17}O spectrum, nine signals were observed that four of them belonged to impurities and the rest were assigned to oxygen at different environments by assist of DFT calculation [29]. They suggested the limited influence of the doping on the overall lattice structure since there is not a significant difference between ^{17}O spectra of LLZO having different amounts of dopants.

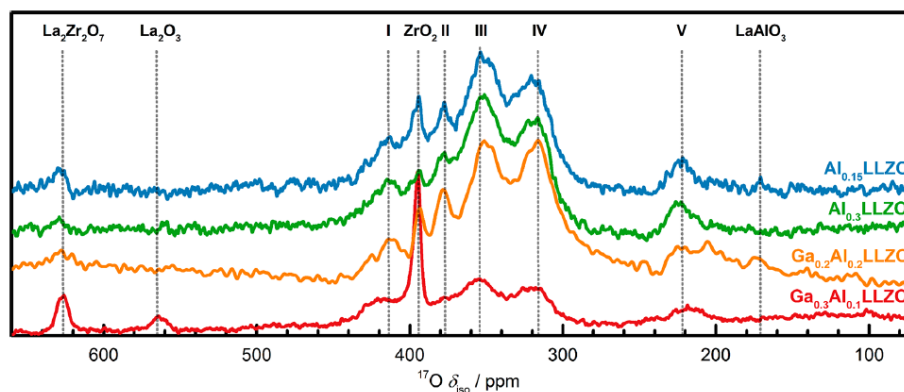


Figure 24. ^{17}O MAS NMR spectra of $\text{Al}^{3+}/\text{Ga}^{3+}$ doped LLZO [29].

1.6. Electrochemical Impedance Spectroscopy (EIS) of LLZOs

The EIS is a powerful tool in determining the charge transfer properties in electrochemical systems. Therefore, researchers have chosen this method to evaluate the ionic conductivity of LLZOs [92]. To perform EIS measurements, the surface of the sintered pellets should be conductive. For this purpose, sputter coating is performed using different types of electrodes such as Au, Pt, Au-Pt, and Carbon. However, Ag and its paste have also been reported [93-96]. EIS measurements are usually performed in the frequency range of 0.1 Hz to 1M Hz with an amplitude ranging from 5 to 100 mV. However, a recent study conducted by Uddin et al. shows that taking into account this large frequency range is unrealistic and the frequency that normal batteries generate is at most about 1000 Hz [97]. The results of EIS measurements are plotted in a Cartesian coordinate system (Nyquist plot) with an X-axis being real impedance (Z_{Re}) and Y-axis being an imaginary one (Z_{Im}). The following graph (**Figure 25**) is the schematic of a typical EIS curve.

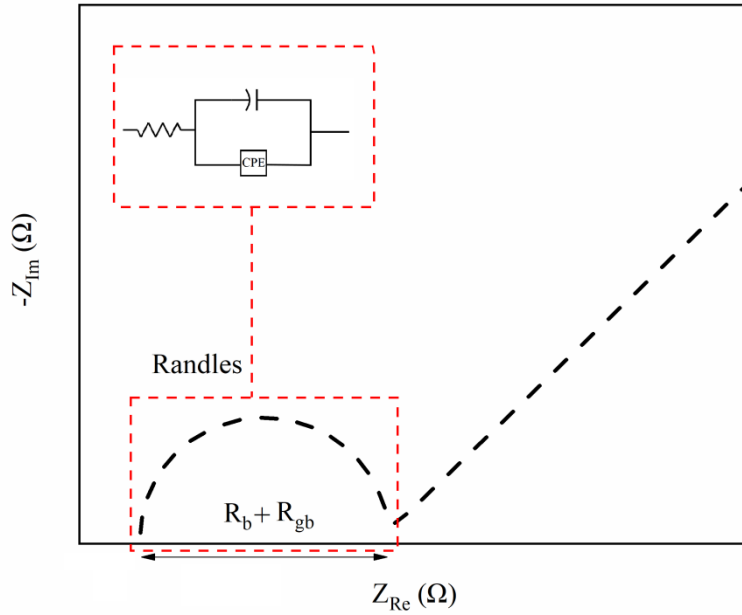


Figure 25. schematic of randle's circuit with bulk (R_b) and grain boundary (R_{gb}) resistance shown on it.

As is seen from the graph, there is a semi-circle and a straight line (tail). It has been reported that high-frequency intercept of the semi-circle with Z_{Re} belongs to bulk and the low-frequency intercept of the semi-circle with Z_{Re} belongs to the grain boundary resistance of LLZO but the real value for resistance is calculated using equivalent circuit [17, 39, 98, 99]. Additionally, when assembling the batteries for LLZO electrolytes, there might appear another semi-circle which is attributed to interfacial resistance between electrode and electrolyte [94]. On the other hand, the tail measured in the low-frequency range stems from the ion blocking electrodes [100, 101]. These semi-circles and tail can be fitted with different equivalent circuits for the actual determination of their resistances [102-104]. The most applicable equivalent circuit is Randle's circuit (illustrated in **Figure 25**) with a tail on it where R_b , R_{gb} , CPE, represent bulk resistance, grain boundary resistance, and constant phase element, respectively [105].

From this circuit, at least two different resistance values are extracted. To check the credibility of the desired circuit, the capacitance derived from the simulation should be plugged into the following equation (1.25) to calculate relative permittivity (ϵ_r) since ϵ_r for LLZO has been calculated to be in 55 to 80 range [20, 106, 107].

$$\epsilon_r = \frac{Cd}{A\epsilon_0} \quad (1.25)$$

Where, ϵ_r , C, d, A, and ϵ_0 denote as relative permittivity, capacitance, thickness, cross-sectional area and permittivity in vacuum ($8.85 \times 10^{-12} \text{ F}\cdot\text{m}^{-1}$), respectively.

These values then are plugged into the following equation to calculate the overall ionic conductivity of the desired electrolyte:

$$\sigma = \frac{d}{R_{(b+gb)} \cdot A} \quad (1.26)$$

Where d is the thickness of pellet, $R_{(b+gb)}$ is the sum of bulk and grain boundary resistances and A is the surface area of the pellet. The dimension of $1/R$ is reported as Seimen (S) and the dimensions of d and A are usually reported in cm and cm^2 scale, respectively, which leads to an overall unit of $\text{S}\cdot\text{cm}^{-1}$. As we discussed earlier in Sec. 1.2, the ionic conduction originates from defects present in LLZO lattice. Therefore, ceramics can only carry charges through movements of ions. The formation of intrinsic defects is dependant on the thermal energy and number of the defects follow an Arrhenius-type equation as below:

$$N_D = N \exp\left(-\frac{E_f}{2kT}\right) \quad (1.27)$$

where N_D is the number of defects, N is the number of ion pairs, E_f is formation energy, k is the Boltzmann constant, and T is the temperature. However, intrinsic defects can attribute less to the ionic conduction. Hence, extrinsic defects are introduced to the structure of LLZO using the incorporation of dopants to improve the ionic conduction. Theoretical ionic conductivity obeys following equation:

$$\sigma = \sum_i q_i N \mu_i \quad (1.28)$$

where q_i is the ionic charge, μ_i is the mobility of ions, and N is the number of mobile defects. When ionic conductivity and diffusion occur by the same mechanism, σ and μ are related to diffusion (D) by the Nernst - Einstein equations as below:

$$\mu = \left(\frac{q}{kT}\right) D \quad (1.29)$$

$$\sigma = \left(\frac{Nq^2}{kT}\right) D \quad (1.30)$$

The above equations represent an idealistic dependence of conductivity on diffusion. However, Carter et al. and Hummel et al. [16, 108] mentioned that:

1. Some defects may contribute to diffusion but not to σ
2. Diffusion can occur along grain boundaries and dislocations. (These are more rapid paths than bulk diffusion).
3. Electronic contributions to σ are low. (especially in wide-band-gap materials at low T).

As it was mentioned above, conductivity falls into two categories: 1) ionic and 2) electronic. The combination of these two exists in LLZO's which can be distinguished by a term called transference number (t). Therefore, the overall conductivity is written as below:

$$\sigma_T = \sigma_I + \sigma_E \quad (1.31)$$

Where σ_T , σ_I , and σ_E are the sum of ionic and electronic conductivity, ionic conductivity and electronic conductivity, respectively.

The contribution of each of these conductivities are written using transference number as below:

$$t_I = \frac{\sigma_I}{\sigma_T} \quad t_E = \frac{\sigma_E}{\sigma_T} \quad (1.32)$$

where t_I and t_E are ionic and electronic transference numbers, respectively. The sum of t_I and t_E is unity [109].

Dependence of ionic conductivity on temperature can be fitted with the Arrhenius equation as below:

$$\sigma_I = \frac{A}{T} \exp\left(-\frac{E_f}{kT}\right) \quad (1.33)$$

From the slope of (3.9), activation energies of Li diffusion can be calculated and this is achievable through the testing of samples at different temperatures.

Most of what we discussed so far in previous sections was to find an understanding of the effect of supervalent dopants on ionic conductivity of LLZO. It was mentioned in earlier sections that each dopant based on where it occupies in LLZO's structure, affects the structure and induces a shift on the ionic conductivity. Now, we will change the trend of discussion

towards the effect of each dopant on the ionic conductivity of LLZO. Hence, the following table compares the effect of each dopant on ionic conductivity LLZO.

Table 3. Summary of the ionic conductivities of aliovalent doped LLZO

X-LLZO	Ionic Conductivity (S.cm ⁻¹)	Structure	S.G	Ref.
LLZO	1×10 ⁻⁶ S.cm ⁻¹	Tetragonal	I41/acd	[8]
Ta-LLZO	5×10 ⁻⁴ S.cm ⁻¹	Cubic	Ia $\bar{3}$ d	[58]
Te-LLZO	1.02×10 ⁻³ S.cm ⁻¹	Cubic	Ia $\bar{3}$ d	[110]
Al-LLZO	4.4×10 ⁻⁶ S.cm ⁻¹	Cubic	Ia $\bar{3}$ d	[13]
Al-LLZO	2×10 ⁻⁴ S.cm ⁻¹	Cubic	Ia $\bar{3}$ d	[111]
Sr-LLZO	5×10 ⁻⁴ S.cm ⁻¹	Cubic	Ia $\bar{3}$ d	[112]
Ga-LLZO	5×10 ⁻⁴ S.cm ⁻¹	Cubic	Ia $\bar{3}$ d	[73]
Al-LLZO	1.9×10 ⁻⁶ S.cm ⁻¹	Cubic	Ia $\bar{3}$ d	[113]
Ge-LLZO	7.63×10 ⁻⁴ S.cm ⁻¹	Cubic	Ia $\bar{3}$ d	[64]
Y-LLZO	9.56×10 ⁻⁴ S.cm ⁻¹	Cubic	Ia $\bar{3}$ d	[114]
Al-LLZO	4×10 ⁻⁴ S.cm ⁻¹	Cubic	Ia $\bar{3}$ d	[37]
Al-LLZO	4×10 ⁻⁴ S.cm ⁻¹	Cubic	Ia $\bar{3}$ d	[115]
Al-LLZO	5.2×10 ⁻⁴ S.cm ⁻¹	Cubic	Ia $\bar{3}$ d	[27]
Fe-LLZO	1.38×10 ⁻³ S.cm ⁻¹	Cubic	I $\bar{4}$ 3d	[20]
Ga-LLZO	1.3×10 ⁻³ S.cm ⁻¹	Cubic	Ia $\bar{3}$ d	[69]
Ga-Y-LLZO	1.61×10 ⁻³ S.cm ⁻¹	Cubic	Ia $\bar{3}$ d	[77]
Al-LLZO	1×10 ⁻³ S.cm ⁻¹	Cubic	Ia $\bar{3}$ d	[80]
Ga-LLZO	1.46×10 ⁻³ S.cm ⁻¹	Cubic	Ia $\bar{3}$ d	[82]
Ge-LLZO	8.28×10 ⁻⁴ S.cm ⁻¹	Cubic	Ia $\bar{3}$ d	[65]
Ge-LLZO	7.63×10 ⁻⁴ S.cm ⁻¹	Cubic	Ia $\bar{3}$ d	[64]
Sb-LLZO	1.53×10 ⁻⁴ S.cm ⁻¹	Cubic	Ia $\bar{3}$ d	[84]
Sb-LLZO	7.7×10 ⁻⁴ S.cm ⁻¹	Cubic	Ia $\bar{3}$ d	[21]
Al-Sb-LLZO	4.1×10 ⁻⁴ S.cm ⁻¹	Cubic	Ia $\bar{3}$ d	[83]
Ga-Ba-Ta-LLZO	1.24×10 ⁻³ S.cm ⁻¹	Cubic	Ia $\bar{3}$ d	[116]
Nb-LLZO	8×10 ⁻⁴ S.cm ⁻¹	Cubic	Ia $\bar{3}$ d	[55]
Ca-Ta-LLZO	3.5×10 ⁻⁴ S.cm ⁻¹	Cubic	Ia $\bar{3}$ d	[48]
Ga-Sc-LLZO	1.8×10 ⁻³ S.cm ⁻¹	Cubic	Ia $\bar{3}$ d	[9]
Al-LLZO	4.48×10 ⁻⁴ S.cm ⁻¹	Cubic	Ia $\bar{3}$ d	[44]

The above results reveal that the trend of an increase in ionic conductivity of LLZO has been promising during recent years in which the value of conductivity has started with 10⁻⁶ S.cm⁻¹ for tetragonal structure and finally has reached to more than 10⁻³ S.cm⁻¹ for the cubic structure and still is increasing. For instance, Bernuy-Lopez et al. [9] demonstrated that Li⁺ ion conductivity of Ga³⁺ doped LLZO can reach up to ~1.3×10⁻³ S. cm⁻¹ at room temperature, which is twice as high as that of Al³⁺ doped LLZO. Moreover, the results of Wagner et al [20]. showed that Fe³⁺ doped LLZO is even applicable for low-temperature environments (lower than 273 K). **Figure 26** demonstrates the impedance spectra of Fe³⁺ doped LLZO at different temperatures. As is seen from this Figure, the resistance of Fe³⁺ doped LLZO is temperature dependant. This much high ionic conductivity is reported to be

caused by structural change in LLZO by doping Fe^{3+} in which it shifts the structure from centric cubic ($\text{Ia}\bar{3}\text{d}$) to the acentric cubic ($\text{I}\bar{4}3\text{d}$).

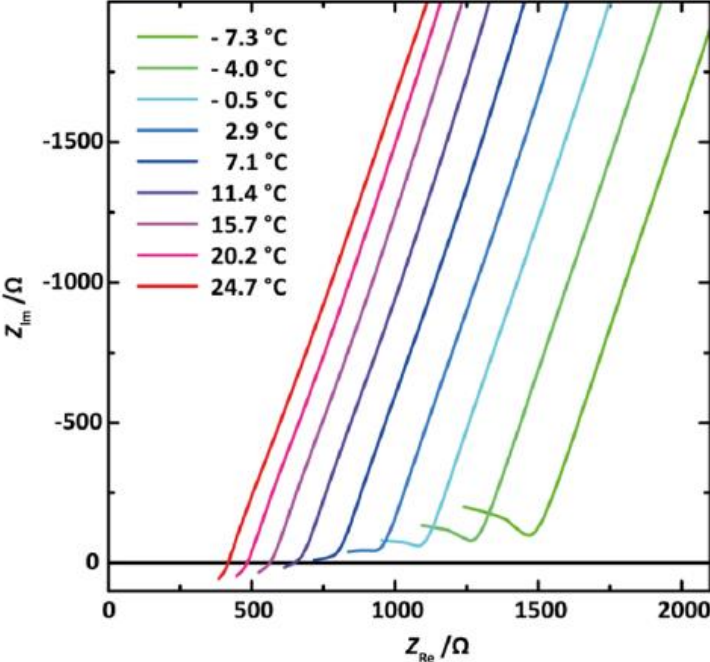


Figure 26. Impedance spectra of Fe^{3+} doped LLZO at various temperatures [20].

Objectives of this thesis

2. Objectives of the Thesis

The engineering of ionic conductivity of $\text{Li}_7\text{La}_3\text{Zr}_2\text{O}_{12}$ compound through addition of dysprosium element, which is used as a solid electrolyte for Li-ion batteries, was the main objective of this thesis. The following features were expected (and were considered) while developing this material:

- Determination of site preference of Dy
- Obtaining crystallographic data of Dy doped LLZO structure (cif file)
- Determining chemical environment of Li ions
- Proposing Li diffusion pathway in the crystal structure
- calculating standard enthalpy of formation for crystal structures through DFT
- Prediction of band structures through DFT
- Obtaining higher ionic conductivity

Materials and methods

3. Materials and methods

3.1. Synthesis

Conventional high-temperature solid-state reaction method was used to prepare samples. For this purpose, ZrO_2 with a purity of 99% (Sigma Aldrich CAS Number: 1314-23-4), La_2O_3 with a purity of 99.9 % (Sigma Aldrich CAS Number: 1312-81-8), Li_2O with a purity of 99.99% (Sigma Aldrich CAS Number: 12057-24-8) and $\text{Dy}(\text{NO}_3)_3 \cdot 5\text{H}_2\text{O}$ with a purity of 99.9% (Alfa Aesar CAS Number: 10031-49-9) were employed. Various Dy-LLZO compositions with the Dy concentrations of 0.1, 0.2, 0.4, and 0.8 pfu with an excess 10% Li_2O (to compensate for Li^+ loss during heat treatment) were weighed and mixed thoroughly in an agate mortar prior to ball milling. Next, each composition was mixed with 50 ml ethanol, poured into a Teflon cup along with zirconia balls and milled for 1 h with a rotational speed of 300 rpm. The milled products were then dried at 100 °C overnight. Subsequently, prepared powders were cold pressed under 20 Mpa in a stainless steel mold with an internal diameter of 12 mm. In the sintering stage, to prevent contamination coming from crucibles, some amount of Dy-LLZO mother powder was put into the alumina crucible, pellets were placed on top of it and then covered again with the mother powder. To further prevent the evaporation of Li during sintering, an alumina lid was placed on top of the crucible. Our sintering steps had two main stages. First, the furnace temperature was raised to 900 °C during 90 min with a dwell time of 10 h and let it cool down naturally to the ambient temperature. Then, for the sake of homogeneity, the pellets underwent ball milling for the second time to increase the reactivity. Next, the temperature was taken to 1000 °C again in 120 min with a dwell time of 1 h.

3.2. Computational method

For the DFT-based total energy calculations and structure optimization, we used the CASTEP code with norm-conserving pseudopotentials for all atoms. The valence shells contain electrons in the following orbitals: 2s1 for Li, 6s24f1 for La, 4f105s25p66s2 for Dy, 4s24p64d25s2 for Zr, 2s22p4 for O atoms. The mesh of the Brillouin zone was set with an actual space of less than 0.03 Å⁻¹. The energy threshold, the maximum atomic displacement, the maximum atomic force and the lattice stress were set to 0.001 meV per atom, 0.0005 Å, 0.01 eV/Å, and 0.02 GPa, respectively. We used the Perdew-Burke-Ernzerhof96 (PBE) and the generalized gradient form (GGA) of the exchange-correlation functional. The NVT ensemble at T = 273.15 K was used for the molecular dynamics check calculations. The Reflex powder diffraction module, implemented in Materials Studio 2016 was used to simulate the XRD pattern of the optimized structures and for the Rietveld refinement of the experimental X-ray powder diffraction pattern by using the optimized Dy-substitute structure.

3.3. Characterization

3.3.1. PXRD

For PXRD measurements, pellets were crushed in an agate mortar and sieved to obtain a finer powder. Measurements were taken with D2 phaser Bruker Advance benchtop diffractometer equipped with a Lynxeye solid-state detector using Cu-K α radiation with a wavelength of 0.154060 nm. For Rietveld refinement purpose, PXRD data were collected at 2 θ positions of ranging from 5° to 90° with a very short step size (0.004 s⁻¹). However, for the normal phase analysis of the samples, 2 θ data were collected from 5° to 90° with a step size of 0.02 s⁻¹. The Rietveld refinement analysis of PXRD data was carried out using Fullprof software and visualization of the structures were carried out by VESTA software.

3.3.2. MAS NMR

The chemical environment and dynamics of Li⁺ for x=0.2 sample were probed by ⁶Li and ⁷Li MAS NMR technique. Solid-state MAS NMR spectra were gathered at room temperature in a Larmor frequency of 73.578 (⁶Li) and 194.317 (⁷Li) MHz using Varian Unity Inova 500MHz Spectrometer (11.7 T) using 4 mm MAS probe with a sample spinning speed of 12 kHz for both nuclei. The ⁶Li and ⁷Li MAS NMR measurements were set to have a pulse duration of 4 μ s along with a recycle delay of 10 s and 20 s respectively. ⁷Li spin lattice relaxation (SLR) in the laboratory frame was characterized by the inversion recovery method with a recycle delay of 40 s and SLR in the rotating frame were recorded using spin-lock technique with a pulsed locking frequency 33.3 kHz, under MAS. ⁷Li spin-spin (or transverse) relaxation (SSR) measurement were recorded by using spin-echo pulse sequence under MAS. Reference chemical shift values, δ_{iso} , were calibrated to 0.1M LiCl aqueous solutions.

3.3.3. FESEM

The morphology of Li₇La₃Dy_xZr_{2-x}O₁₂ at x=0.2 was obtained using Zeiss LEO Supra 35 VP SEM-FEG equipped with an Energy Dispersive X-ray spectroscopy (EDS) operating at 30 kV. For this purpose, pellets were crushed and ball milled for 24 hours with a rate of 300 rpm to minimize the particle size. Furthermore, particles were sputter-coated with the Au-Pt electrode for 60s.

3.3.4. ICP

Since Li⁺ is not detectable by EDS, inductively coupled plasma optical emission spectrometer (Vista-Pro Axial, Varian Pty Ltd, Mulgrave, Australia) elemental analysis method was used to measure the Li⁺ amount in the Li₇La₃Dy_xZr_{2-x}O₁₂ at x=0.2. Before ICP measurements, Li₇La₃Dy_xZr_{2-x}O₁₂ at x=0.2 was crushed and digested in a diluted HNO₃ (30%) acid solution and microwave treated for 30 minutes to assure the complete dissociation of ions in the solution.

3.3.5. EIS

The ionic conductivity measurements were performed by Biologic VMP-3 Galvanostat/Potentiostat in a frequency range of 1 MHz to 1 Hz and a signal amplitude of 50 mV. The pellets were first polished and tailored to the diameter of 10 mm and then coated with the Au-Pt on both sides for 120 s. A copper cell was designed and fabricated to minimize the resistance which contributes to the overall impedance of the system (Cell + Pellet).

Results and discussions

4. Results and discussions

4.1. PXRD of samples

The $\text{Li}_7\text{La}_3\text{Dy}_x\text{Zr}_{2-x}\text{O}_{12}$ pellets sintered at 1273 K resulted in a single-phase for $x = 0.1, 0.2, 0.4$, as shown in the X-ray powder diffraction measurements in **Figure 27a**. At higher content of dysprosium, in particular for $x = 0.8$, an impurity phase was detected, which can be assigned to the pyrochlore phase $\text{La}_2\text{Zr}_2\text{O}_7$, as shown in **Figure 27b**. Further analysis of the patterns confirms the presence of the centric space group of $I\bar{3}ad$ (No. 230) in pure cubic samples ($x = 0.1, 0.2$, and 0.4). This symmetry is in good agreement with the results obtained for Al^{3+} doped LLZO by other research groups [13, 19, 45, 115].

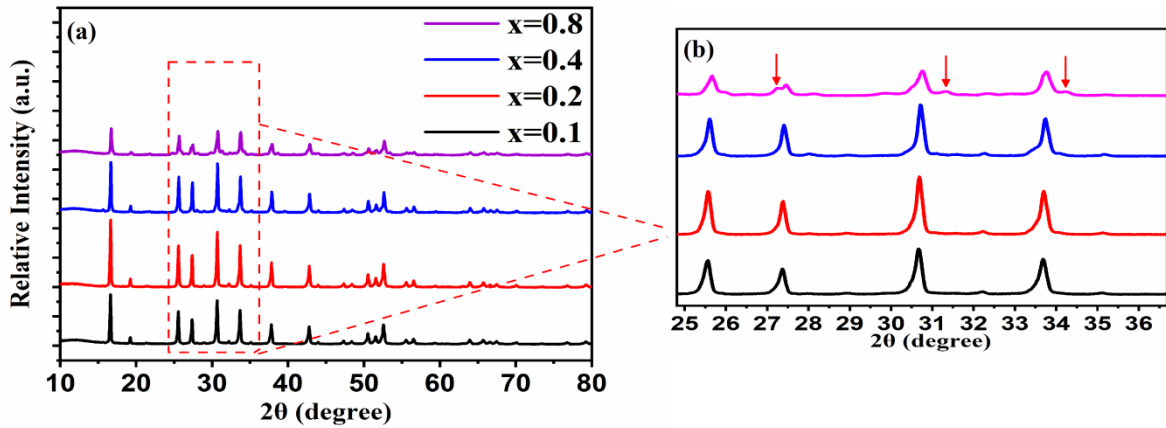


Figure 27. (a) X-ray powder diffraction patterns of $\text{Li}_7\text{La}_3\text{Dy}_x\text{Zr}_{2-x}\text{O}_{12}$ at different composition. (b) The impurity phase diffraction peaks occurring at high Dy content, assigned to the formation of pyrochlore phase $\text{La}_2\text{Zr}_2\text{O}_7$.

The garnet prototype $\text{Ca}_3\text{Al}_2[\text{SiO}_4]_3$ ($Z = 8$) has Ca atoms on 24c sites in $(1/8, 0, 1/4)$ with square antiprism O_8 coordination, Al atoms on 16a sites in $(0, 0, 0)$ with octahedral O_6 coordination, Si atoms on 24d sites in $(3/8, 0, 1/4)$ with tetrahedral O_4 coordination, and O atoms on 96h sites in $(0.09869, 0.20477, 0.28825)$.

By using the garnet prototype as a template structure, we built the initial cubic structure for the DFT calculations. Accordingly, La atoms were placed on the 24c sites; Zr atoms on 16a sites; Li atoms on 24d sites and O atoms left in the 96h sites. An addition of 32 atoms of Li were located on 32e sites in (x, x, x) , with $x = 1/8$, in order to reach the stoichiometry of LLZO, though their occupancy brings Li atoms to a relatively short distance (about 1.53 \AA) for an initial choice of the lattice parameter of 13.00 \AA .

In the cubic structure reported in the literature, for example in Li atoms are located on 96h and 24d sites with occupancy of 0.360 and 0.692, respectively, for a total of 6.396 atoms of Li per formula unit. The choice of 96h site brings Li atoms too close, about 0.89 \AA apart, for which we did not consider that structure as a possible starting structure in our DFT calculations. In addition, the initial structure for the calculations should at best locate the

atoms on the Wyckoff sites with full occupancy. Therefore, the structure proposed in [71] though it is not suitable as an initial structure for the calculations, it provides the idea that the 96h sites might not represent local minima sites. Other possible sites are, in principle, available to Li atoms in the cubic Ia-3d lattice. They are the 12a (3/8,0,1/4), 16b (x,x,x), 48f (0,0,1/4), 48g (1/8,y, -y+1/4) sites, with an initial choice for example of x = 1/8 and y = 0.08.

The 12a (3/8,0,1/4) and 48f (0,0,1/4) sites are mentioned in Ga-LLZO [81] for $\text{Li}_{7-3x}\text{Ga}_{3x}\text{La}_3\text{Zr}_2\text{O}_{12}$, with $x > 0.07$; while for example in Ta-LLZO [57, 73] it is mentioned the possibility for Li atoms to occupy the 48g sites in (1/4, 0, 0). In ICSD's Crystal Data, of the ten entries reported with cubic structures, three of them locate Li atoms also on the 48g sites with partial occupancy of 0.333, in addition to 24d and 96h sites, also partially occupied.

In order to check changes in site preference upon composition, we modelled two structures with Li atoms located on fully occupied 48f sites for the composition $\text{Li}_6\text{La}_3\text{Zr}_2\text{O}_{12}$ and 24d and 32e sites for $\text{Li}_7\text{La}_3\text{Zr}_2\text{O}_{12}$. Our molecular dynamics simulations at 300 K using the NVT ensemble of $\text{Li}_7\text{La}_3\text{Zr}_2\text{O}_{12}$ suggest that actually Li atoms move along the voids in a sort of site percolation and that the sites (24d) – (48g) – (96h) proposed in the literature with different occupancies represent the dynamical path through which Li atoms move. This reinforces the idea that the very close 96h sites, experimentally suggested being partially occupied, are only dynamically visited by Li atoms, and that all possible voids are somehow visited depending on the sample temperature and the exact amount of Li in the lattice.

The calculated enthalpy of formation, though it does not include the zero-point energy and the thermal contribution at the moment -- which might be derived from the phonon dispersion calculations -- indicates, as expected from the experiments, that the tetragonal structure is thermodynamically more stable than the cubic by 24.5 kJ/mol, being the calculated enthalpies of formation -7198.3 kJ/mol and -7173.8 kJ/mol respectively for the tetragonal and the cubic structures of LLZO. In addition, the comparison of the enthalpies of formation of $\text{Li}_6\text{La}_3\text{Zr}_2\text{O}_{12}$ and $\text{Li}_7\text{La}_3\text{Zr}_2\text{O}_{12}$ indicates that the addition of one mole of Li stabilizes the cubic structure of LLZO by 112 kJ/mol. The experimentally reported standard enthalpy of formation of $\text{Li}_7\text{La}_3\text{Zr}_2\text{O}_{12}$ is -7152.6 kJ/mol [117]. In **Table 4** we report the structure data and the calculated enthalpies of formation.

Table 4. Standard enthalpies of formation for different compounds of this work derived from DFT computations.

Compound	Formula	$\Delta_f H$ [KJ/mol]	Space group	a^* (Å)	b^* (Å)	c^* (Å)	$V^\#(\text{Å}^3)$
LLZO	$\text{Li}_6\text{La}_3\text{Zr}_2\text{O}_{12}$	-5817.50	$\text{Ia}\bar{3}\text{d}$	12.9539	12.9539	12.9539	2173.7103
LLZO	$\text{Li}_6\text{La}_3\text{Zr}_2\text{O}_{12}$	-6824.83	$\bar{\text{I}}\bar{4}3\text{d}$	12.3793	12.3793	12.3793	1897.0915
LLZO	$\text{Li}_7\text{La}_3\text{Zr}_2\text{O}_{12}$	-7198.30	I41/acd	12.49560	12.48140	12.47460	1945.5511
Dy-LLZO	$\text{Li}_6\text{La}_3\text{Dy}_{0.125}\text{Zr}_{1.875}\text{O}_{12}$	-6749.93	P 1	12.42900	12.43100	12.42720	1920.0592
LLZO	$\text{Li}_7\text{La}_3\text{Zr}_2\text{O}_{12}$	-7173.80	P 1	12.48570	12.47390	12.47130	1942.3391
Dy-LLZO	$\text{Li}_7\text{La}_3\text{Dy}_{0.125}\text{Zr}_{1.875}\text{O}_{12}$	-7024.35	P 1	12.49560	12.48140	12.47460	1945.5511
Dy-LLZO	$\text{Li}_{6.5}\text{Dy}_{0.25}\text{La}_3\text{Zr}_2\text{O}_{12}$	-6551.50	P 1	12.49560	12.48140	12.47460	1945.5511
Dy-LLZO	$\text{Li}_{6.75}\text{Dy}_{0.125}\text{La}_3\text{Zr}_2\text{O}_{12}$	-6724.90	P 1	12.49560	12.48140	12.47460	1945.5511

*Lattice parameters
#Cellvolume

4.2.Dy-substitute LLZO

For the Dy-substituted LLZO, the possibility that Dy atoms substitute La atoms is ruled out on the basis of the lattice parameter dependence on composition, shown in **Figure 1**, where the lattice parameters, were obtained via the Rietveld refinement (using FullPROF program) of the low-resolution X-ray powder patterns. The linear dependence of the lattice parameter, which follows the Vegard's law, indicates a lattice expansion on increasing the Dy content. A possible substitution of La atoms by Dy atoms would lead instead to a decrease of the lattice parameter as increasing x, because of the lanthanide contraction, being the ionic radius of Dy(III) smaller than that of La(III). Moreover, the substitution of Li atom by Dy atoms could lead to a decrease of the Li content, which was not analytically observed ($\text{Li}_{6.960}\text{La}_3\text{Dy}_{0.244}\text{Zr}_{1.756}\text{O}_{12}$).

Therefore, Dy atoms could substitute Zr atoms, and be either homogeneously distributed on Zr sites, which then become partially occupied and preserving the symmetry, or completely substitute (occupation = 1) some of the 16a sites, and accordingly breaking the symmetry.

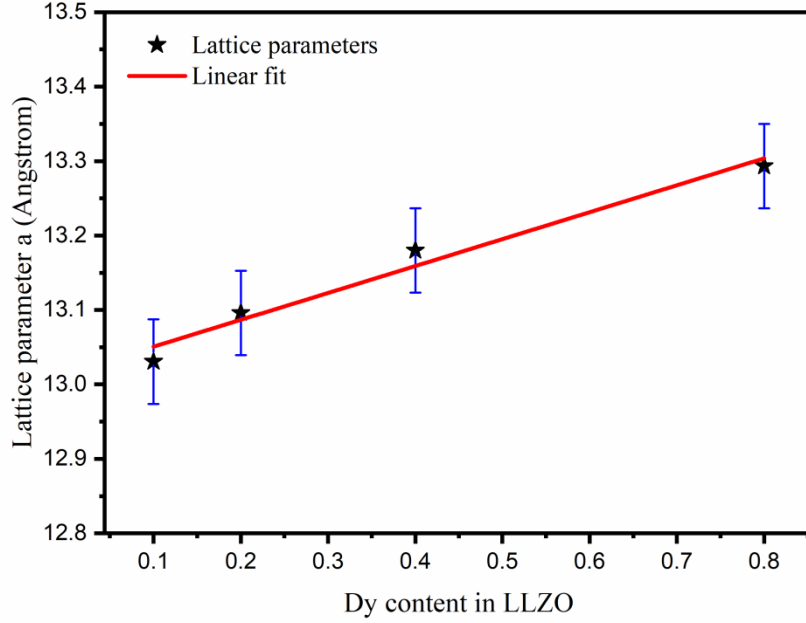
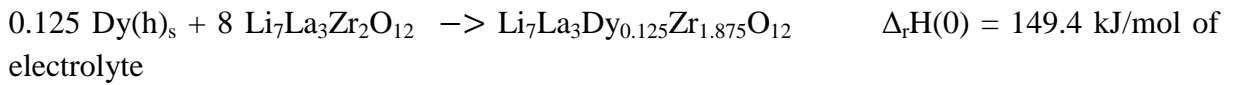
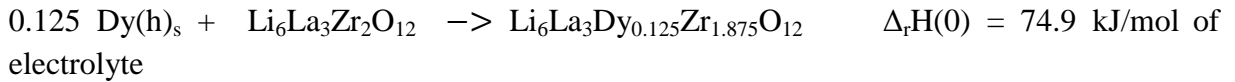


Figure 18. Variation of lattice parameter as a function of Dy content in $\text{Li}_7\text{La}_3\text{Dy}_x\text{Zr}_{2-x}\text{O}_{12}$.

The results of the full geometry optimization of $\text{Li}_6\text{La}_3\text{Dy}_{0.125}\text{Zr}_{1.875}\text{O}_{12}$ and $\text{Li}_7\text{La}_3\text{Dy}_{0.125}\text{Zr}_{1.875}\text{O}_{12}$, with one Dy atom on a Zr site (one of the 16a sites with occupancy equal to 1) suggest that the formation is thermodynamically possible and that the calculated enthalpies of formation are -6749.9 kJ/mol and -7024.4 kJ/mol, respectively. Correspondingly, the reaction of Dy-substitution is an endothermic process with the calculated enthalpies of reactions:



The calculated X-ray diffraction pattern of the refined structure overlaid with the experimental pattern of the sample with $x = 0.2$ is shown in **Figure 29**, and the crystallographic data obtained via Rietveld refinement are reported in **Table 5**.

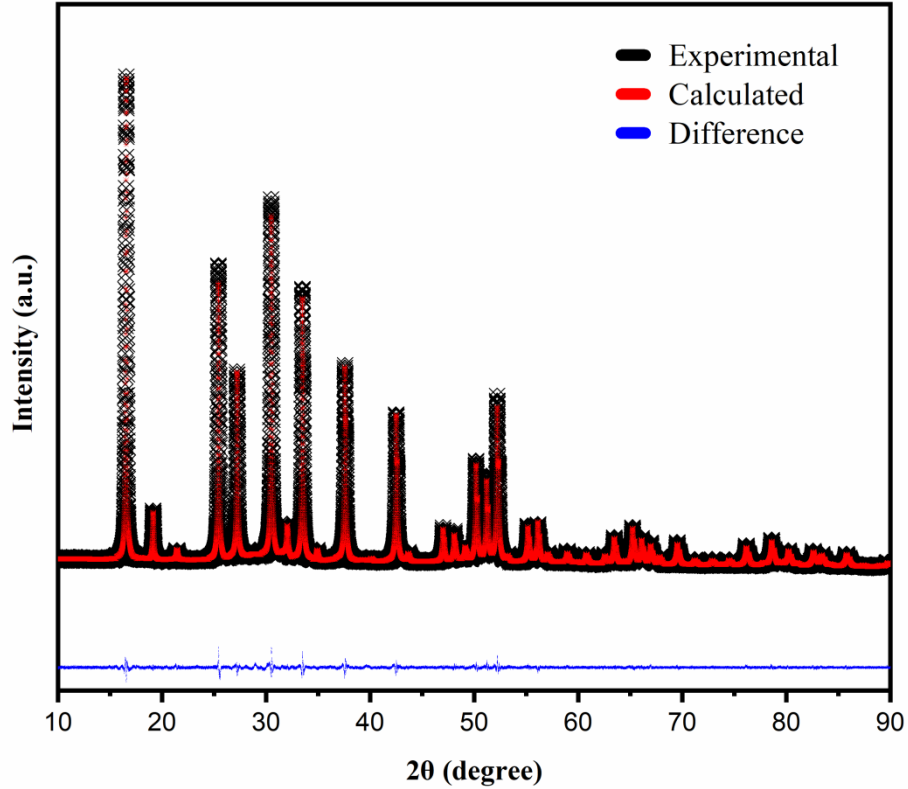


Figure 29. Experimental and calculated patterns of $\text{Li}_7\text{La}_3\text{Dy}_x\text{Zr}_{2-x}\text{O}_{12}$ at $x=0.2$ from rietveld refinement

Table 5. Coordination, occupancy, thermal factor and site preference of different atoms for LLZO at $x=0.2$ pfu are demonstrated.

Atom	Symbol	x	y	z	Occupancy	U	Site
O	O1	0.09984	0.19471	0.27574	1.000	0.031	96h
La	La1	0.12500	0.00000	0.25000	1.000	0.019	24c
Zr	Zr1	0.00000	0.00000	0.00000	0.880	0.059	16a
Li	Li1	0.37500	0.00000	0.2500	0.550	0.496	24d
Li	Li2	0.12500	0.32890	-0.07890	0.880	0.046	48g
Dy	Dy1	0.00000	0.00000	0.00000	0.121	0.059	16a

Space Group: $\text{Ia}\bar{3}\text{d}$ (#230)

$a = 13.09620 \text{ \AA}$ $b = 13.09620 \text{ \AA}$ $c = 13.09620 \text{ \AA}$

$\alpha = 90^\circ$ $\beta = 90^\circ$ $\gamma = 90^\circ$

$V = 2246.1352 \text{ \AA}^3$

$\chi^2 = 2.76\%$ $R_{wp} = 8.79\%$

The lattice parameter difference between the optimized structure and the refined structure is mainly to be ascribed to the particular computational settings and the intrinsic discrepancy observed between the calculated and the experimental values. **Figure 30** demonstrates polyhedral volume of Dy doped LLZO. As seen, three dimensional pathway for Li ions (Blue and pink atoms) is developed when Dy is doped in LLZO structure. Such a Li configuration ensures faster Li movement providing higher ionic conductivity.

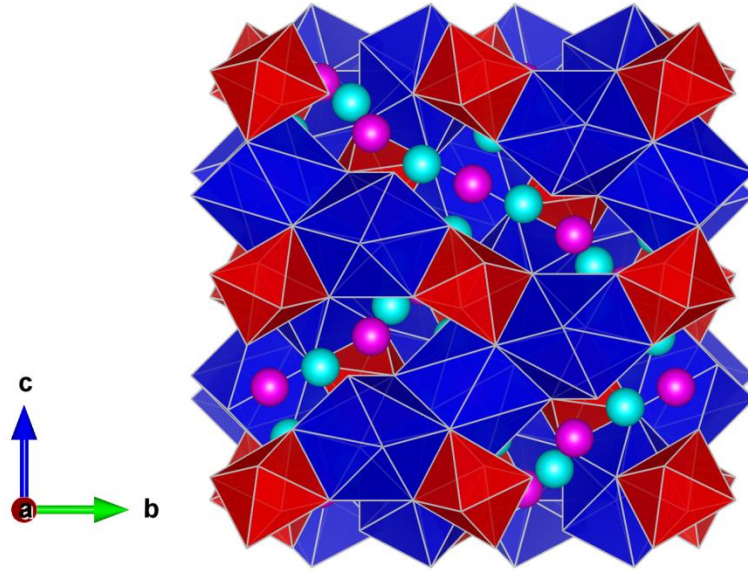


Figure 30. demonstrates the polyhedral model of Dy-LLZO structure

4.3. Bonding features

Although its inherent limitations and a lack of a numerically precise agreement with the experimentally determined values, the comparison of the band gap between the Dy-LLZO and LLZO can help to investigate the electronic effects of the Dy substitution and get more information, though mainly qualitatively, about the chemical environment of Dy atom.

The comparison of the calculated band structures of the Dy-LLZO and LLZO suggest that one Dy atom per unit cell can shift down the band by about 0.7 eV and provide donor states at the Fermi level. Consequently, the band gap decreases by 3.74 eV, passing from 4.075 eV in LLZO to 0.331 in Dy-LLZO. The partial density of states, the projected density of states and the orbitals analysis indicate that the additional states are brought in by Dy atoms and that they are predominantly of f-orbital character. In **Figure 31** and **32**, the band structure of substituted and unsubstituted LLZO is reported together with the partial density of states.

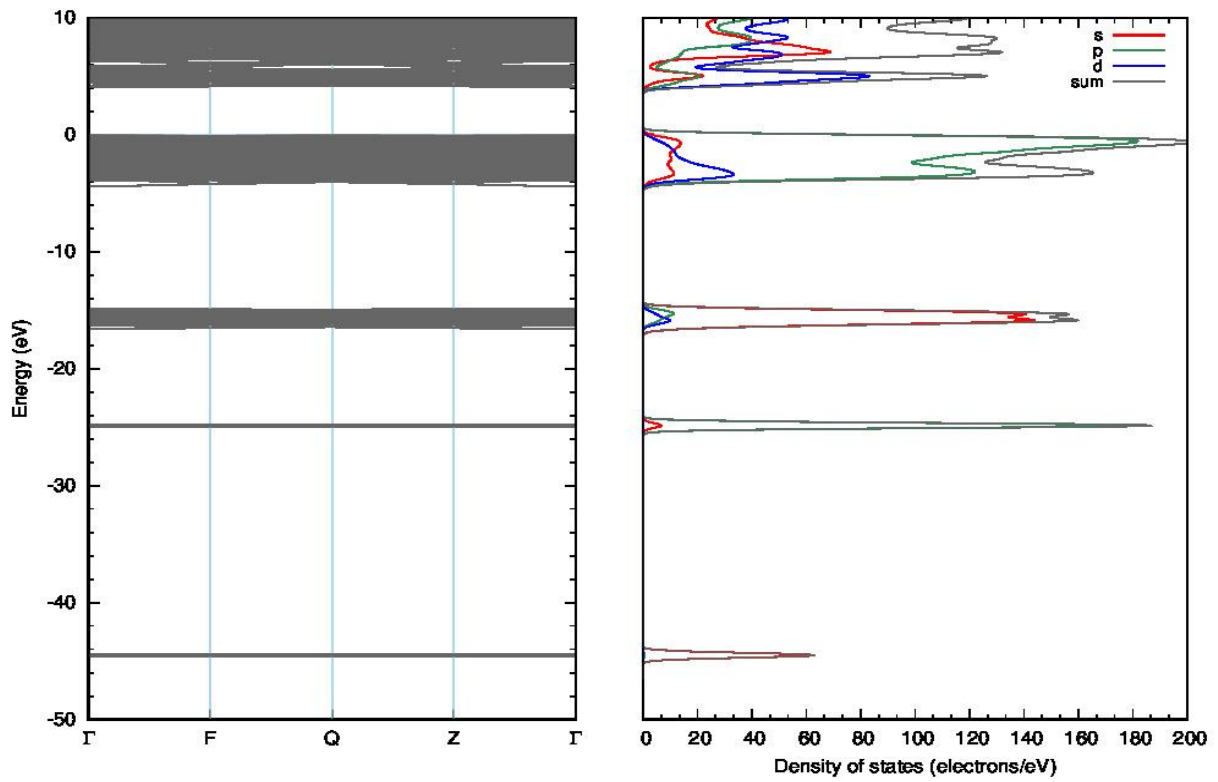


Figure 31. The band structure and the partial density of states of undoped LLZO.

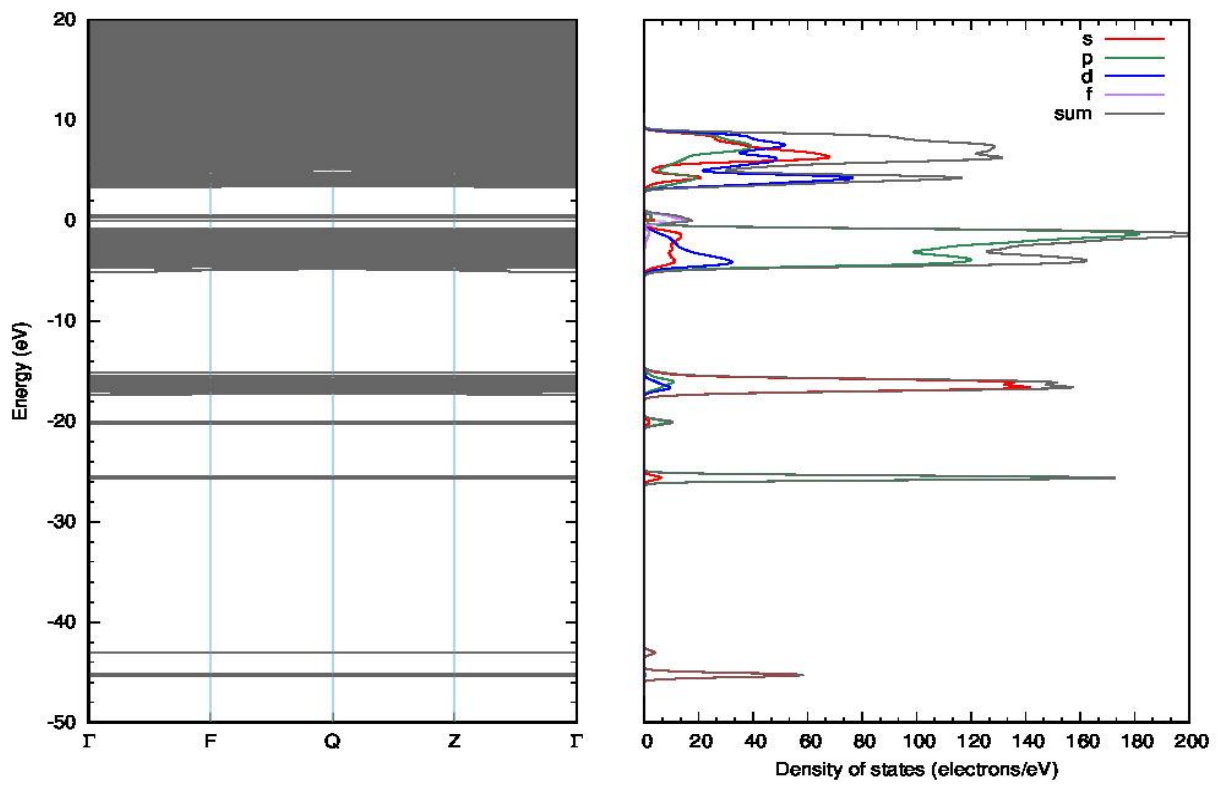
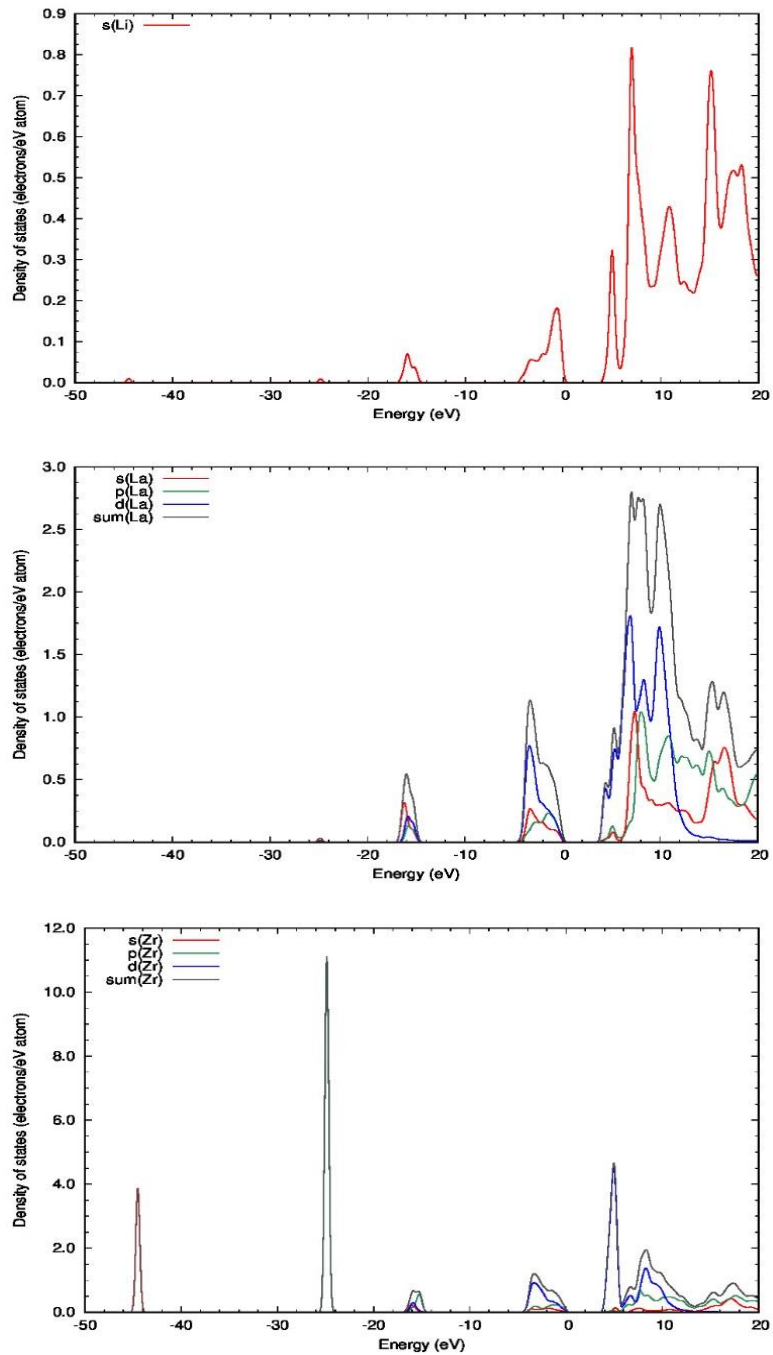


Figure 32. The band structure and the partial density of states of Dy doped LLZO.

In **Figure 33** and **34**, the projected density of states of undoped LLZO and Dy doped LLZO are divided by the number of each species and show the s-, p-, d-, f-type contributions of each atoms to the band structure, respectively.



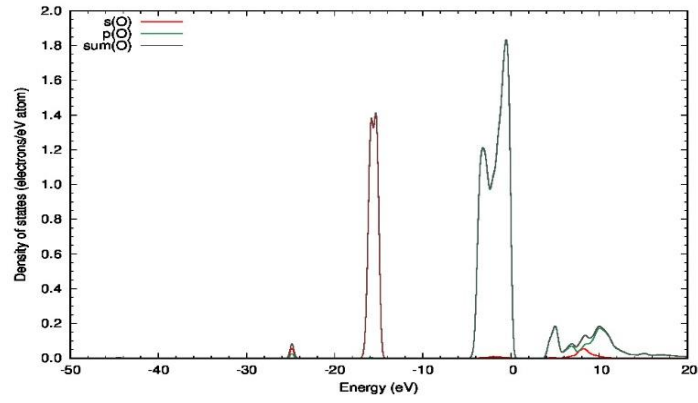


Figure 33. Projected density of states of undoped LLZO.

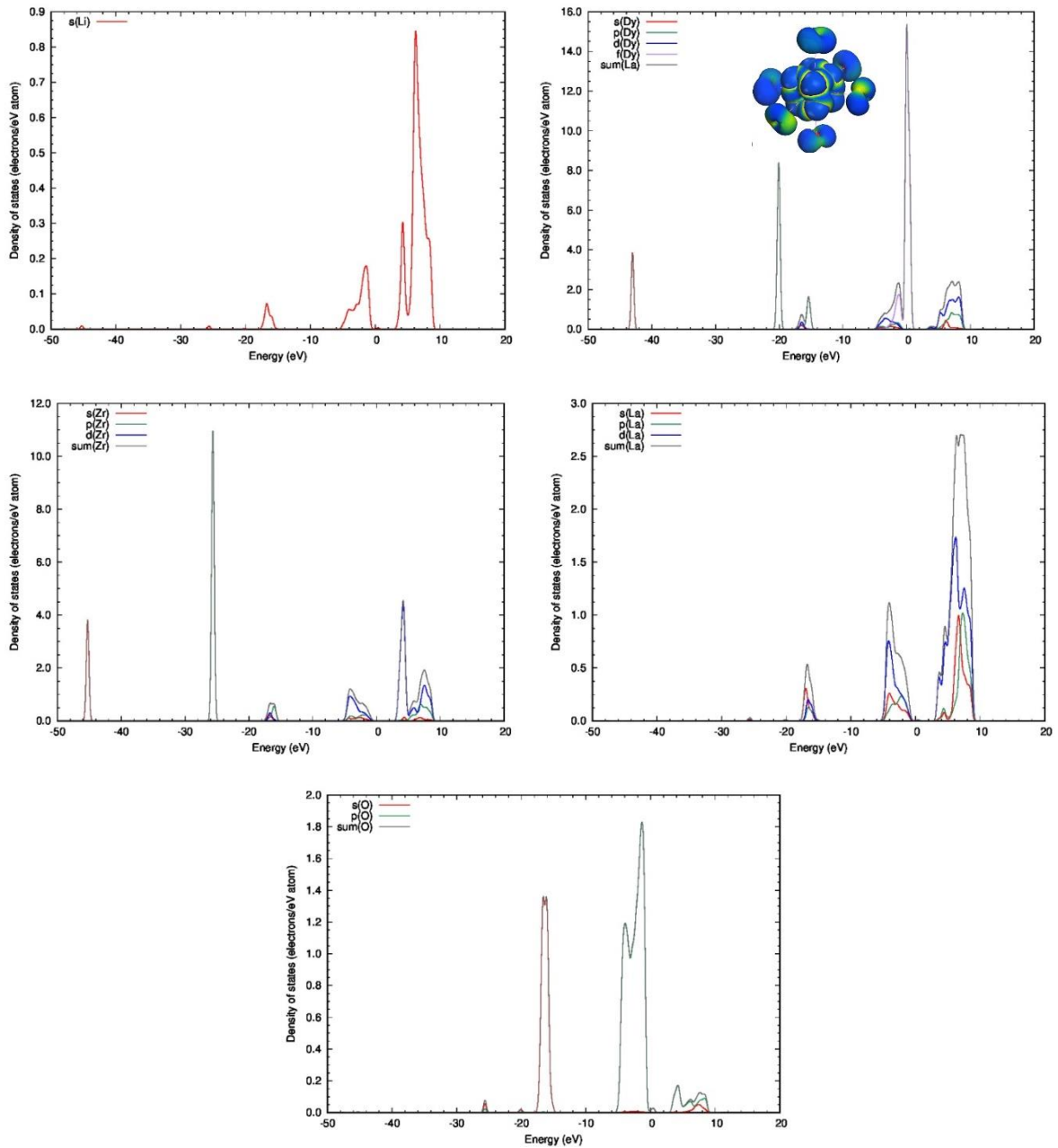


Figure 34. Projected density of states of Dy doped LLZO. An isodensity surface showing the f-p character of the Dy-O bonding is shown in the Dy-PDOS panel.

Clearly, in LLZO the f-orbitals of La are not bonding orbitals as La is present as cation, while in Dy-LLZO, the 4f orbitals do participate to the bonding, and being partially occupied, they provide bonding/antibonding states at the Fermi level, decreasing the band gap consequently.

4.4. ${}^7\text{Li}$ and ${}^6\text{Li}$ MAS NMR

The ${}^7\text{Li}$ ($I = 3/2$) and ${}^6\text{Li}$ ($I = 1$) with the natural abundance of 92.58% 7.42%, respectively [89], are quadrupolar and highly dependent on the interaction of surrounding electric field gradient and their relevant quadrupolar moment (-4×10^{-2} and -8×10^{-4} , respectively) [79]. Therefore, such nuclei have lower symmetry and give rise to a central line flanked with two satellite transitions [90]. Since the nuclei are quadrupolar, the NMR spectrum of ${}^7\text{Li}$ is expected to appear broader due to the rapid relaxation. The broadening of the line is also a sign of the presence of asymmetry. This broadening arises from a larger distribution and diversity of chemical environments (Li occupying different sites) with a higher rate of disorder surrounding the Li cations [9]. Additionally, the shape of the central transitions provides a sense of the distribution of Li jump rates and Li migration pathways in garnets [90]. There is a strong correlation between Li solid-state NMR chemical shifts and the local environment of the garnet structure. This capability in NMR can provide us the information about the coordination number of Li and also the number of sites that Li occupies in the structure.

The MAS NMR spectrum of ${}^7\text{Li}$ of the $\text{Li}_7\text{La}_3\text{Dy}_x\text{Zr}_{2-x}\text{O}_{12}$ at $x=0.2$ is shown in Fig 8a. ${}^7\text{Li}$ spectrum demonstrates a narrower band with the highest intensity located at the ~ 1.7 ppm and includes two rotational sidebands. As ${}^7\text{Li}$ has a spin $3/2$ nucleus, its NMR line has a central line ($+1/2 \rightleftharpoons -1/2$) and satellite shoulders which stem from the spin-transitions of $+3/2 \rightleftharpoons -3/2$. Since the signals from different sites of the Li are overlapped, this limits the access to further structural information such as the chemical environment and site preference of Li^+ ions. However, based on the literature, this resonance belongs to the lithium at the octahedral site (48g) [106].

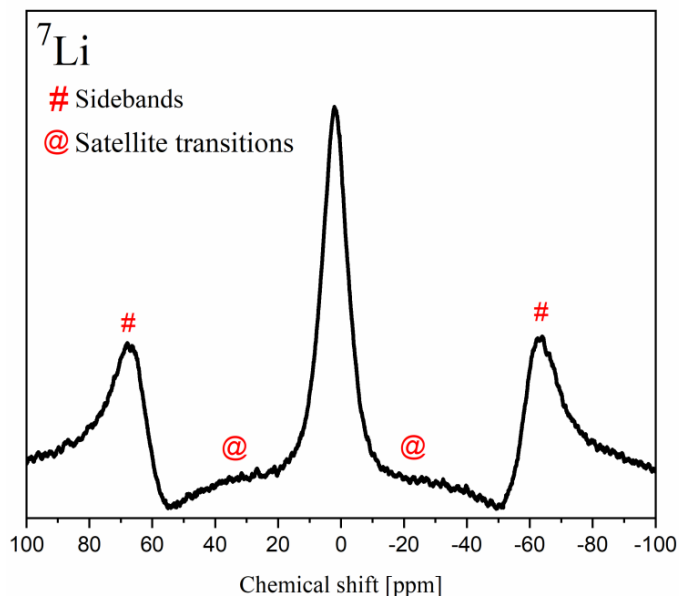


Figure 35. ${}^7\text{Li}$ MAS NMR spectrum of $\text{Li}_7\text{La}_3\text{Dy}_x\text{Zr}_{2-x}\text{O}_{12}$ at $x=0.2$ recorded at 273 K

Therefore, the need for a ${}^6\text{Li}$ measurement seems to be mandatory to distinguish these signals. Hence, we measured and obtained the MAS NMR spectrum of ${}^6\text{Li}$ for $\text{Li}_7\text{La}_3\text{Dy}_x\text{Zr}_{2-x}\text{O}_{12}$ at $x=0.2$ sample at 273 K and it is shown in **Figure 36**. ${}^6\text{Li}$ the spectrum exhibits a narrow central line with two overlapped resonances on it which is a sign of faster Li hopping rates at this temperature [32]. The spectral decomposition of the NMR spectrum of ${}^6\text{Li}$ reveals two resonance peaks at ~ 0.7 ppm and ~ 1.7 ppm. The peak located at 0.7 ppm is very close to the typical chemical shift of the tetrahedral site and this has been confirmed by many authors [82, 106, 118]. The other resonance positioned at 1.7 ppm is also close to the chemical shift of the octahedral site (48g) [82] which has been extensively studied and proposed by other research groups and agrees well with the resonance signal obtained above for ${}^7\text{Li}$. Since in both cases (${}^6\text{Li}$ and ${}^7\text{Li}$) the line shapes obey a gaussian function, a larger portion of the Li ions participates in the diffusion process which is a sign of higher mobility of Li ions in Dy doped LLZO and therefore higher ionic conductivity of $\text{Li}_7\text{La}_3\text{Dy}_x\text{Zr}_{2-x}\text{O}_{12}$ at $x=0.2$ [90, 119]. These narrow lines can be further sharpened with increasing temperature since at higher temperatures both magnetic dipole-dipole interactions and electric quadrupolar interactions are dramatically averaged. However, we limit our investigation to only room temperature in this study.

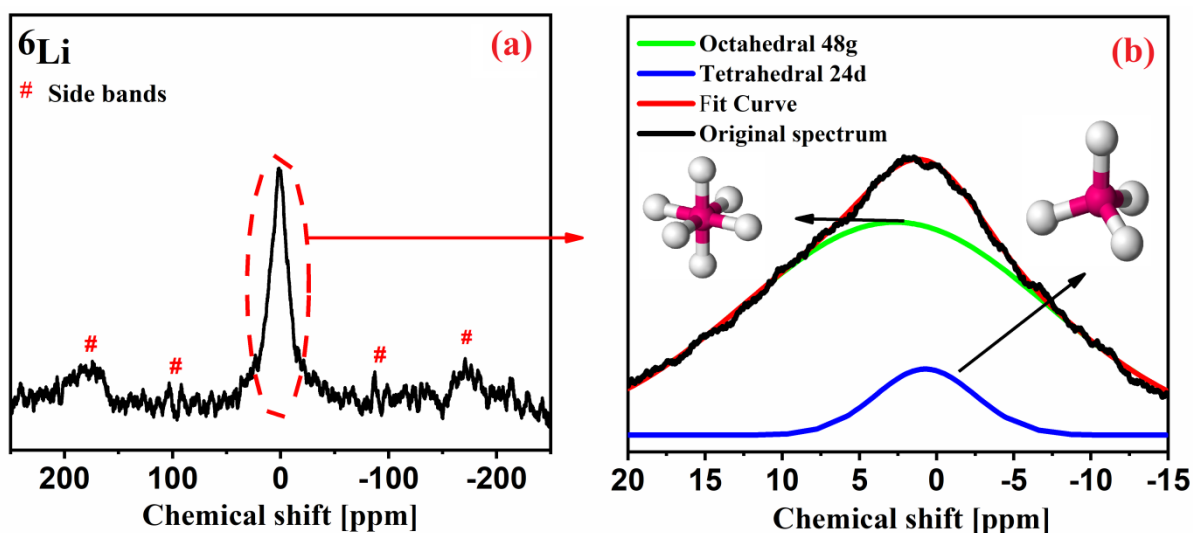


Figure 36. (a) The MAS ${}^6\text{Li}$ NMR spectrum of $\text{Li}_7\text{La}_3\text{Dy}_x\text{Zr}_{2-x}\text{O}_{12}$ at $x=0.2$ at 273 K. (b) The deconvoluted partial MAS NMR spectrum of ${}^6\text{Li}$.

To obtain further insight into Li dynamics of Dy doped LLZO, saturation recovery experiment was carried out. Fortunately, the spin-lattice relaxation method is highly sensitive to the local environment of Li ions. The graph demonstrated in **Figure 37** shows roughly a homogeneous behavior, however, it could only be fitted with a biexponential function and a single exponential did not give a good result. Therefore, two different T_1 values were extracted from the biexponential function ($T_1^\alpha = \sim 0.15\text{ s}$ and $T_1^\beta = \sim 25.4\text{ s}$) which are attributed to two different Li sites in the structure. The shorter one, $T_1^\alpha = \sim 0.15\text{ s}$, is ascribed to the Li ions in 6-fold coordination and the longer one, $T_1^\beta = \sim 25.4\text{ s}$, belongs to the Li ions in 4-fold coordination. Such a short value at the octahedral (48g) site is a sign of higher mobility at this void.

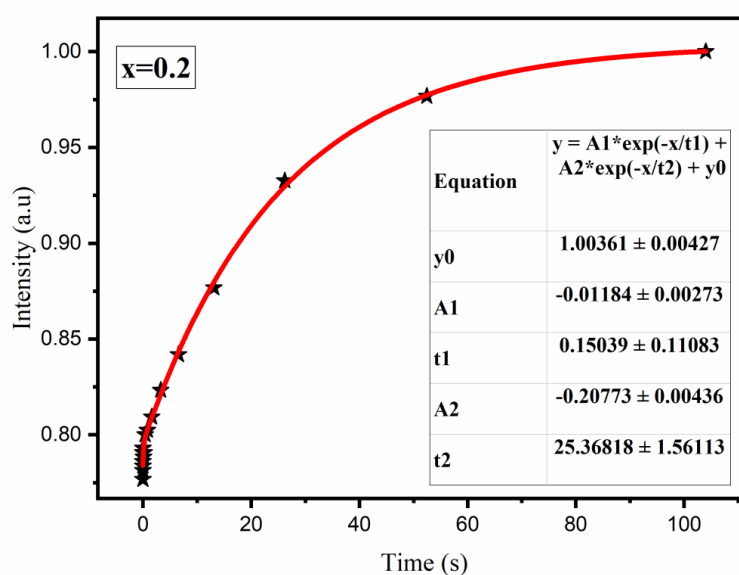


Figure 37. T_1 relaxations curve of ${}^7\text{Li}$ for $x=0.2$ at 273.15 K

4.5. Ionic conductivity measurements

The EIS method was carried out to unveil the effect of Dy concentration on the ionic conductivity of the samples. For this purpose, impedance spectra of all the samples were recorded in frequency range of 1Hz to 1MHz with a signal amplitude of 50 mV at 296 K and are illustrated in **Figure 38a, b, c, and d** and also the equivalent fitted plot of $\text{Li}_7\text{La}_3\text{Dy}_x\text{Zr}_{2-x}\text{O}_{12}$ at $x=0.2$ is shown in **Figure 39**. It is clearly seen from the Nyquist plots in **Figure 38** that all the resistance values are below 500 Ω . Additionally, the plots show only bulk resistances at high-frequency part due to the lack of a complete semi-circle and a dramatic steep rise towards imaginary parts at the low frequencies which itself arises from ionically blocking electrodes (Au-Pd). To precisely determine the resistance values of the spectra, different equivalent circuits were examined and serial combination of inductance (L) to two resistances (R) which themselves were separately assembled parallel to two constant phase elements (CPE_1 and CPE_2) serial to another CPE_3 element was employed to assemble the equivalent circuit. The overall circuit is demonstrated in **Figure 39**. The simulated equivalent circuit indicated χ^2 value of 0.00025 which is considered as excellent fit. Therefore, the values of resistance along with pellet dimensions were plugged into the following equation to estimate the bulk ionic conductivity of the samples and the results are all reported in **Table 6**.

$$\sigma = \frac{d}{R.A} \quad (4-1)$$

Where d is the thickness of pellet, R is bulk resistance and A is the cross-sectional area of the pellet.

In the case of the LLZOs, specific capacitance for bulk and grain boundary conductivities are in the range of 10^{-11} to 10^{-12} F and 10^{-8} to 10^{-11} F, respectively [106, 107, 120]. To check the validity of the proposed circuit, the capacitance derived from the simulation was plugged to the following equation (1) to calculate the relative permittivity (ϵ_r).

$$\epsilon_r = \frac{Cd}{A\epsilon_0} \quad (4-2)$$

Where ϵ_r , C , d , A , and ϵ_0 denote as the relative permittivity, capacitance, thickness, cross sectional area and permittivity in vacuum ($8.85 \times 10^{-12} \text{ F}\cdot\text{m}^{-1}$), respectively. The result of calculation led to $\epsilon_r = 78.6 \text{ F}\cdot\text{m}^{-1}$ which is in the range LLZOs.

Table 6. Calculated ionic conductivities for Dy=0.1, 0.2, 0.4, and 0.8 pfu in LLZO through fitting of EIS spectra by equivalent circuit.

Sample	Bulk Resistance (Ω)	Thickness (mm)	Diameter (mm)	Bulk conductivity S.cm^{-1}
$\text{Li}_7\text{Dy}_{0.1}\text{La}_3\text{Zr}_{1.9}\text{O}_{12}$	145	1.54	1	1.35×10^{-3}
$\text{Li}_7\text{Dy}_{0.2}\text{La}_3\text{Zr}_{1.8}\text{O}_{12}$	107	1.71	1	2.03×10^{-3}
$\text{Li}_7\text{Dy}_{0.4}\text{La}_3\text{Zr}_{1.6}\text{O}_{12}$	200	1.63	1	1.03×10^{-3}
$\text{Li}_7\text{Dy}_{0.8}\text{La}_3\text{Zr}_{1.2}\text{O}_{12}$	287	1.49	1	6.32×10^{-4}

As a result of increasing Dy concentration, first, the bulk ionic conductivity increased up to the 0.2 pfu Dy and then decreased by increasing the Dy content (shown in **Figure 40**). This is probably due to occurrence of the minor phase separation and development of the pyrochlore phase in the material. To our knowledge, the obtained ionic conductivity in this study for $\text{Li}_7\text{Dy}_{0.2}\text{La}_3\text{Zr}_{1.8}\text{O}_{12}$ is the highest value reported up to now for LLZOs at room temperature.

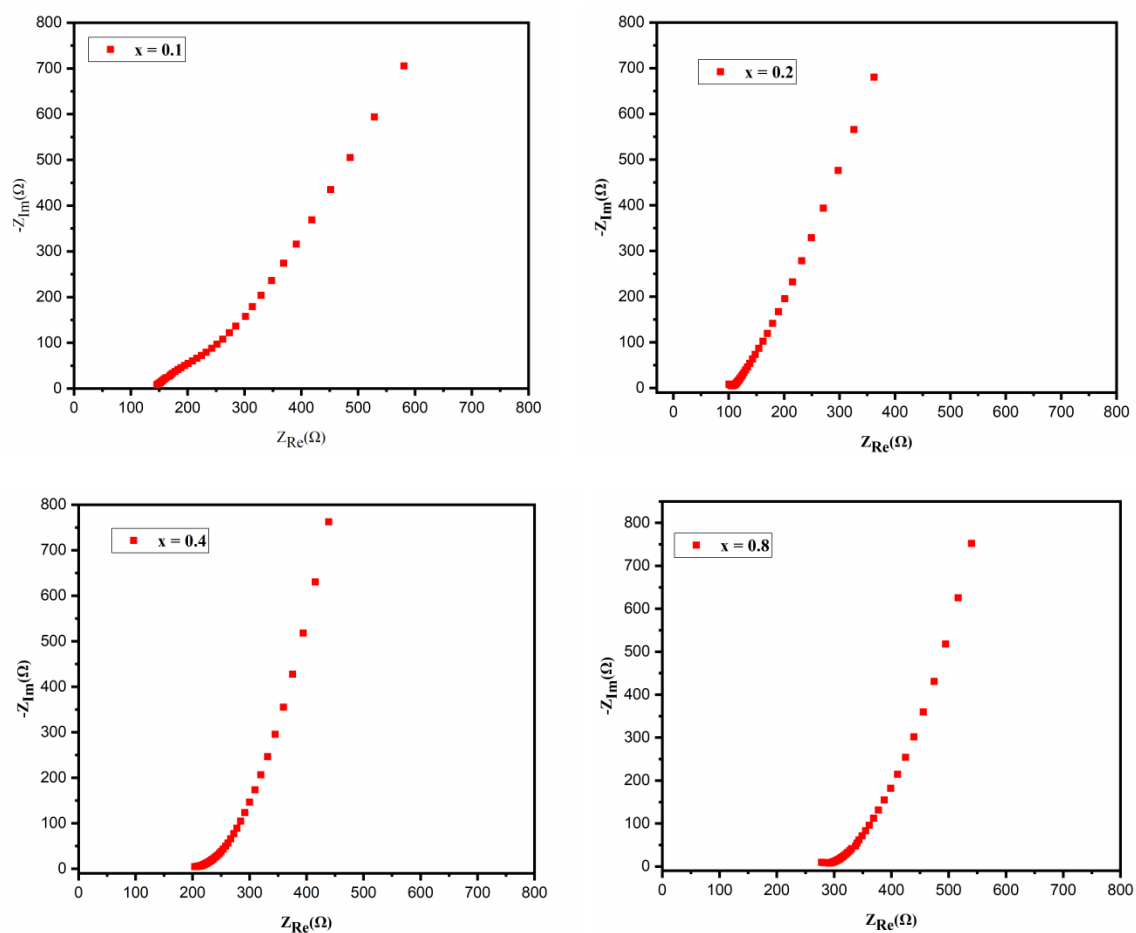


Figure 38. EIS spectra of $\text{Li}_7\text{La}_3\text{Dy}_x\text{Zr}_{2-x}\text{O}_{12}$ at (a) $x=0.1$, (b) $x=0.2$, (c) $x=0.4$, and (d) $x=0.8$

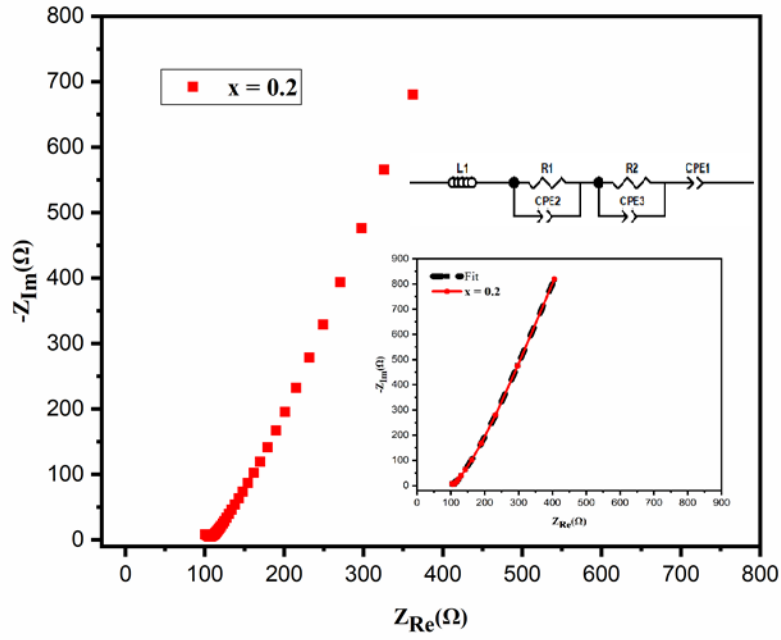


Figure 39. Fitted plot impedance spectrum along with equivalent circuit for $\text{Li}_7\text{La}_3\text{Dy}_x\text{Zr}_{2-x}\text{O}_{12}$ at $x=0.2$.

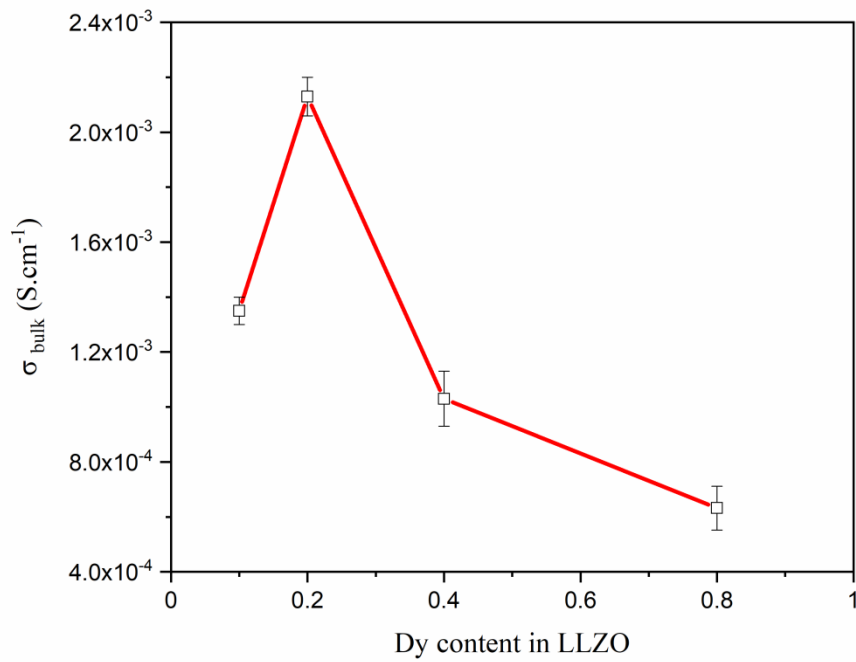


Figure 40. Effect of Dy content on the ionic conductivity of LLZO.

Conclusion

5. Conclusion

In this study, we have demonstrated that dysprosium can be employed to transform the tetragonal $\text{Li}_7\text{La}_3\text{Zr}_2\text{O}_{12}$ into cubic, thereby increasing the ionic conductivity of it dramatically ($2.03 \times 10^{-3} \text{ S.cm}^{-1}$). To investigate the possible reasons behind such an increase in ionic conductivity, we explored the crystal structure both experimentally and computationally. Through X-ray diffraction and solid-state NMR coupled with total energy DFT calculations, it was found that Dy could probably occupy Zr site with preserving the Ia d symmetry. When doping Dy at Zr site, the lowest standard enthalpy of formation for cubic symmetry was achieved which helped us develop and obtain the structure from Rietveld refinement calculations.

Increasing the Dy content above 0.2 pfu did not give any good results causing the structure to undergo phase separation, thereby, decreasing the ionic conductivity. the final structure demonstrate that Li moves through 24d–96h–48g pathway. However, molecular dynamic results demonstrated that 96h site is only dynamically visited providing no minima energetically.

Our solid electrolyte with superior properties can be employed in all-solid-state batteries and function properly.

References

1. Henriksen, M., et al., *Explosion characteristics for Li-ion battery electrolytes at elevated temperatures*. Journal of hazardous materials, 2019. **371**: p. 1-7.
2. Mehraeen, S., et al., *Homogeneous growth of TiO₂-based nanotubes on nitrogen-doped reduced graphene oxide and its enhanced performance as a Li-ion battery anode*. Nanotechnology, 2018. **29**(25): p. 255402.
3. Zheng, F., et al., *Review on solid electrolytes for all-solid-state lithium-ion batteries*. Journal of Power Sources, 2018. **389**: p. 198-213.
4. Sharafi, A., et al., *Characterizing the Li–Li₇La₃Zr₂O₁₂ interface stability and kinetics as a function of temperature and current density*. Journal of Power Sources, 2016. **302**: p. 135-139.
5. Meier, K., T. Laino, and A. Curioni, *Solid-state electrolytes: revealing the mechanisms of Li-ion conduction in tetragonal and cubic LLZO by first-principles calculations*. The Journal of Physical Chemistry C, 2014. **118**(13): p. 6668-6679.
6. Ohta, S., et al., *Electrochemical performance of an all-solid-state lithium ion battery with garnet-type oxide electrolyte*. Journal of Power Sources, 2012. **202**: p. 332-335.
7. Teng, S., J. Tan, and A. Tiwari, *Recent developments in garnet based solid state electrolytes for thin film batteries*. Current Opinion in Solid State and Materials Science, 2014. **18**(1): p. 29-38.
8. Murugan, R., V. Thangadurai, and W. Weppner, *Fast lithium ion conduction in garnet-type Li₇La₃Zr₂O₁₂*. Angewandte Chemie International Edition, 2007. **46**(41): p. 7778-7781.
9. Buannic, L., et al., *Dual substitution strategy to enhance Li⁺ ionic conductivity in Li₇La₃Zr₂O₁₂ solid electrolyte*. Chemistry of materials, 2017. **29**(4): p. 1769-1778.
10. Wang, M. and J. Sakamoto, *Correlating the interface resistance and surface adhesion of the Li metal-solid electrolyte interface*. Journal of Power Sources, 2018. **377**: p. 7-11.
11. Ni, J.E., et al., *Room temperature elastic moduli and Vickers hardness of hot-pressed LLZO cubic garnet*. Journal of Materials Science, 2012. **47**(23): p. 7978-7985.
12. Wolfenstine, J., et al., *Mechanical behavior of Li-ion-conducting crystalline oxide-based solid electrolytes: a brief review*. Ionics, 2018. **24**(5): p. 1271-1276.
13. Djenadic, R., et al., *Nebulized spray pyrolysis of Al-doped Li₇La₃Zr₂O₁₂ solid electrolyte for battery applications*. Solid State Ionics, 2014. **263**: p. 49-56.
14. Cussen, E.J., *Structure and ionic conductivity in lithium garnets*. Journal of Materials Chemistry, 2010. **20**(25): p. 5167-5173.
15. Miara, L.J., et al., *Effect of Rb and Ta Doping on the Ionic Conductivity and Stability of the Garnet Li₇(La_{3-x}Rb_x)(Zr_{2-y}Ta_y)O₁₂ (0 ≤ x ≤ 0.375, 0 ≤ y ≤ 1) Superionic Conductor: A First Principles Investigation*. 2013.
16. Carter, C.B. and M.G. Norton, *Ceramic materials: science and engineering*. Vol. 716. 2007: Springer.
17. Wolfenstine, J., et al., *High conductivity of dense tetragonal Li₇La₃Zr₂O₁₂*. Journal of Power Sources, 2012. **208**: p. 193-196.
18. Bernstein, N., M. Johannes, and K. Hoang, *Origin of the structural phase transition in Li₇La₃Zr₂O₁₂*. Physical review letters, 2012. **109**(20): p. 205702.
19. Chen, Y.-T., et al., *Voltammetric Enhancement of Li-Ion Conduction in Al-Doped Li_{7-x}La₃Zr₂O₁₂ Solid Electrolyte*. The Journal of Physical Chemistry C, 2017. **121**(29): p. 15565-15573.
20. Wagner, R., et al., *Fast Li-Ion-Conducting Garnet-Related Li_{7-3xFex}La₃Zr₂O₁₂ with Uncommon I43d Structure*. Chemistry of Materials, 2016. **28**(16): p. 5943-5951.
21. Ramakumar, S., et al., *Structure and Li⁺ dynamics of Sb-doped Li₇La₃Zr₂O₁₂ fast lithium ion conductors*. Physical Chemistry Chemical Physics, 2013. **15**(27): p. 11327-11338.

22. Mois Ilia, A., et al., *Bilbao Crystallographic Server: I. Databases and crystallographic computing programs*. Zeitschrift für Kristallographie - Crystalline Materials, 2006. **221**(1): p. 15-27.
23. Zhan, X., et al., *Defect chemistry and electrical properties of garnet-type $\text{Li}_7\text{La}_3\text{Zr}_2\text{O}_{12}$* . Physical Chemistry Chemical Physics, 2018. **20**(3): p. 1447-1459.
24. Moradabadi, A. and P. Kaghazchi, *Defect chemistry in cubic $\text{Li}_6.25\text{Al}_0.25\text{La}_3\text{Zr}_2\text{O}_{12}$ solid electrolyte: A density functional theory study*. Solid State Ionics, 2019. **338**: p. 74-79.
25. Thompson, T., et al., *Tetragonal vs. cubic phase stability in Al-free Ta doped $\text{Li}_7\text{La}_3\text{Zr}_2\text{O}_{12}$ (LLZO)*. Journal of Materials Chemistry A, 2014. **2**(33): p. 13431-13436.
26. Santosh, K., et al., *Point defects in garnet-type solid electrolyte (c- $\text{Li}_7\text{La}_3\text{Zr}_2\text{O}_{12}$) for Li-ion batteries*. Solid State Ionics, 2014. **261**: p. 100-105.
27. Cheng, L., et al., *Effect of microstructure and surface impurity segregation on the electrical and electrochemical properties of dense Al-substituted $\text{Li}_7\text{La}_3\text{Zr}_2\text{O}_{12}$* . Journal of Materials Chemistry A, 2014. **2**(1): p. 172-181.
28. Shin, D.O., et al., *Synergistic multi-doping effects on the $\text{Li}_7\text{La}_3\text{Zr}_2\text{O}_{12}$ solid electrolyte for fast lithium ion conduction*. Scientific reports, 2015. **5**: p. 18053.
29. Karasulu, B., et al., *Al/Ga-Doped $\text{Li}_7\text{La}_3\text{Zr}_2\text{O}_{12}$ Garnets as Li-Ion Solid-State Battery Electrolytes: Atomistic Insights into Local Coordination Environments and Their Influence on ^{17}O , ^{27}Al , and ^{71}Ga NMR Spectra*. Journal of the American Chemical Society, 2020. **142**(6): p. 3132-3148.
30. Paoletta, A., et al., *Discovering the Influence of Lithium Loss on Garnet $\text{Li}_7\text{La}_3\text{Zr}_2\text{O}_{12}$ Electrolyte Phase Stability*. ACS Applied Energy Materials, 2020.
31. Geiger, C.A., et al., *Crystal chemistry and stability of " $\text{Li}_7\text{La}_3\text{Zr}_2\text{O}_{12}$ " garnet: a fast lithium-ion conductor*. Inorganic chemistry, 2011. **50**(3): p. 1089-1097.
32. Kuhn, A., et al., *Li self-diffusion in garnet-type $\text{Li}_7\text{La}_3\text{Zr}_2\text{O}_{12}$ as probed directly by diffusion-induced Li_7 spin-lattice relaxation NMR spectroscopy*. Physical Review B, 2011. **83**(9): p. 094302.
33. Thompson, T., et al., *A tale of two sites: on defining the carrier concentration in garnet-based ionic conductors for advanced Li batteries*. Advanced Energy Materials, 2015. **5**(11): p. 1500096.
34. Posch, P., et al., *Ion dynamics in Al-Stabilized $\text{Li}_7\text{La}_3\text{Zr}_2\text{O}_{12}$ single crystals—Macroscopic transport and the elementary steps of ion hopping*. Energy Storage Materials, 2020. **24**: p. 220-228.
35. Liu, K., et al., *Trace element and REE geochemistry of the Zhewang gold deposit, southeastern Guizhou Province, China*. Chinese Journal of Geochemistry, 2014. **33**(1): p. 109-118.
36. Zhang, Y., et al., *Effect of lithium ion concentration on the microstructure evolution and its association with the ionic conductivity of cubic garnet-type nominal $\text{Li}_7\text{Al}_0.25\text{La}_3\text{Zr}_2\text{O}_{12}$ solid electrolytes*. Solid State Ionics, 2016. **284**: p. 53-60.
37. Rangasamy, E., J. Wolfenstine, and J. Sakamoto, *The role of Al and Li concentration on the formation of cubic garnet solid electrolyte of nominal composition $\text{Li}_7\text{La}_3\text{Zr}_2\text{O}_{12}$* . Solid State Ionics, 2012. **206**: p. 28-32.
38. Im, C., et al., *Al-incorporation into $\text{Li}_7\text{La}_3\text{Zr}_2\text{O}_{12}$ solid electrolyte keeping stabilized cubic phase for all-solid-state Li batteries*. Journal of energy chemistry, 2018. **27**(5): p. 1501-1508.
39. David, I.N., et al., *Microstructure and Li-Ion Conductivity of Hot-Pressed Cubic $\text{Li}_7\text{La}_3\text{Zr}_2\text{O}_{12}$* . Journal of the American Ceramic Society, 2015. **98**(4): p. 1209-1214.
40. Allen, J.L., et al., *Effect of substitution (Ta, Al, Ga) on the conductivity of $\text{Li}_7\text{La}_3\text{Zr}_2\text{O}_{12}$* . Journal of Power Sources, 2012. **206**: p. 315-319.
41. Kumazaki, S., et al., *High lithium ion conductive $\text{Li}_7\text{La}_3\text{Zr}_2\text{O}_{12}$ by inclusion of both Al and Si*. Electrochemistry communications, 2011. **13**(5): p. 509-512.
42. Xie, H., et al., *Lithium distribution in aluminum-free cubic $\text{Li}_7\text{La}_3\text{Zr}_2\text{O}_{12}$* . Chemistry of Materials, 2011. **23**(16): p. 3587-3589.

43. Kotobuki, M., et al., *Fabrication of all-solid-state lithium battery with lithium metal anode using Al₂O₃-added Li₇La₃Zr₂O₁₂ solid electrolyte*. Journal of Power Sources, 2011. **196**(18): p. 7750-7754.
44. Xia, W., et al., *Ionic conductivity and air stability of Al-doped Li₇La₃Zr₂O₁₂ sintered in alumina and Pt crucibles*. ACS applied materials & interfaces, 2016. **8**(8): p. 5335-5342.
45. Duvel, A., et al., *Mechanosynthesis of solid electrolytes: preparation, characterization, and Li ion transport properties of garnet-type Al-doped Li₇La₃Zr₂O₁₂ crystallizing with cubic symmetry*. The Journal of Physical Chemistry C, 2012. **116**(29): p. 15192-15202.
46. Shimonishi, Y., et al., *Synthesis of garnet-type Li_{7-x}La₃Zr₂O_{12-1/2x} and its stability in aqueous solutions*. Solid State Ionics, 2011. **183**(1): p. 48-53.
47. Buschmann, H., et al., *Structure and dynamics of the fast lithium ion conductor "Li₇La₃Zr₂O₁₂"*. Physical Chemistry Chemical Physics, 2011. **13**(43): p. 19378-19392.
48. Hubaud, A.A., et al., *Low temperature stabilization of cubic (Li_{7-x}Al_{x/3})La₃Zr₂O₁₂: role of aluminum during formation*. Journal of Materials Chemistry A, 2013. **1**(31): p. 8813-8818.
49. Li, Y., et al., *Densification and ionic-conduction improvement of lithium garnet solid electrolytes by flowing oxygen sintering*. Journal of Power sources, 2014. **248**: p. 642-646.
50. El-Shinawi, H., E.J. Cussen, and S.A. Corr, *Enhancement of the lithium ion conductivity of Ta-doped Li₇La₃Zr₂O₁₂ by incorporation of calcium*. Dalton Transactions, 2017. **46**(29): p. 9415-9419.
51. Cussen, E.J., *The structure of lithium garnets: cation disorder and clustering in a new family of fast Li⁺ conductors*. Chemical Communications, 2006(4): p. 412-413.
52. Murugan, R., V. Thangadurai, and W. Weppner, *Effect of lithium ion content on the lithium ion conductivity of the garnet-like structure Li_{5+x}BaLa₂Ta₂O_{11.5+0.5x} (x=0-2)*. Applied Physics A, 2008. **91**(4): p. 615-620.
53. Murugan, R., V. Thangadurai, and W. Weppner, *Lattice parameter and sintering temperature dependence of bulk and grain-boundary conduction of garnet-like solid Li-electrolytes*. Journal of The Electrochemical Society, 2008. **155**(1): p. A90-A101.
54. Thangadurai, V., S. Adams, and W. Weppner, *Crystal structure revision and identification of Li⁺-ion migration pathways in the garnet-like Li₅La₃M₂O₁₂ (M= Nb, Ta) oxides*. Chemistry of materials, 2004. **16**(16): p. 2998-3006.
55. Ohta, S., T. Kobayashi, and T. Asaoka, *High lithium ionic conductivity in the garnet-type oxide Li_{7-x}La₃(Zr_{2-x}Nb_x)O₁₂ (X=0-2)*. Journal of Power Sources, 2011. **196**(6): p. 3342-3345.
56. Kihira, Y., et al., *Effect of simultaneous substitution of alkali earth metals and Nb in Li₇La₃Zr₂O₁₂ on lithium-ion conductivity*. ECS Electrochemistry Letters, 2013. **2**(7): p. A56-A59.
57. Li, Y., et al., *Optimizing Li⁺ conductivity in a garnet framework*. Journal of Materials Chemistry, 2012. **22**(30): p. 15357-15361.
58. Buschmann, H., et al., *Lithium metal electrode kinetics and ionic conductivity of the solid lithium ion conductors "Li₇La₃Zr₂O₁₂" and Li_{7-x}La₃Zr_{2-x}Ta_xO₁₂ with garnet-type structure*. Journal of Power Sources, 2012. **206**: p. 236-244.
59. Logéat, A., et al., *From order to disorder: The structure of lithium-conducting garnets Li_{7-x}La₃Ta_xZr_{2-x}O₁₂ (x=0-2)*. Solid State Ionics, 2012. **206**: p. 33-38.
60. Wang, Y. and W. Lai, *High ionic conductivity lithium garnet oxides of Li_{7-x}La₃Zr_{2-x}Ta_xO₁₂ compositions*. Electrochemical and Solid State Letters, 2012. **15**(5): p. A68.
61. Inada, R., et al., *Formation and stability of interface between garnet-type Ta-doped Li₇La₃Zr₂O₁₂ solid electrolyte and lithium metal electrode*. Batteries, 2018. **4**(2): p. 26.
62. Percival, J. and P. Slater, *Identification of the Li sites in the Li ion conductor, Li₆SrLa₂Nb₂O₁₂, through neutron powder diffraction studies*. Solid state communications, 2007. **142**(6): p. 355-357.
63. Meesala, Y., et al., *An efficient multi-doping strategy to enhance Li-ion conductivity in the garnet-type solid electrolyte Li₇La₃Zr₂O₁₂*. Journal of materials chemistry A, 2019. **7**(14): p. 8589-8601.

64. Huang, M., A. Dumon, and C.-W. Nan, *Effect of Si, In and Ge doping on high ionic conductivity of Li7La3Zr2O12*. *Electrochemistry communications*, 2012. **21**: p. 62-64.
65. Huang, M., et al., *X-ray absorption near-edge spectroscopy study on Ge-doped Li7La3Zr2O12: enhanced ionic conductivity and defect chemistry*. *Electrochimica Acta*, 2014. **115**: p. 581-586.
66. Peng, H., et al., *Effect of Ge substitution for Nb on Li ion conductivity of Li5La3Nb2O12 solid state electrolyte*. *Electrochimica Acta*, 2017. **251**: p. 482-487.
67. Garcia Daza, F.A., et al., *Atomistic insight into ion transport and conductivity in ga/al-substituted li7la3zr2o12 solid electrolytes*. *ACS applied materials & interfaces*, 2018. **11**(1): p. 753-765.
68. Jalem, R., et al., *Effects of gallium doping in garnet-type Li7La3Zr2O12 solid electrolytes*. *Chemistry of Materials*, 2015. **27**(8): p. 2821-2831.
69. Bernuy-Lopez, C., et al., *Atmosphere controlled processing of Ga-substituted garnets for high Li-ion conductivity ceramics*. *Chemistry of materials*, 2014. **26**(12): p. 3610-3617.
70. Howard, M., et al., *Effect of Ga incorporation on the structure and Li ion conductivity of La3Zr2Li7O12*. *Dalton transactions*, 2012. **41**(39): p. 12048-12053.
71. Rettenwander, D., et al., *Crystal chemistry of "Li7La3Zr2O12" garnet doped with Al, Ga, and Fe: a short review on local structures as revealed by NMR and Mößbauer spectroscopy studies*. *European journal of mineralogy*, 2016. **28**(3): p. 619-629.
72. Rawlence, M., et al., *Effect of Gallium Substitution on Lithium-Ion Conductivity and Phase Evolution in Sputtered Li7-3 x Ga x La3Zr2O12 Thin Films*. *ACS applied materials & interfaces*, 2018. **10**(16): p. 13720-13728.
73. El Shinawi, H. and J. Janek, *Stabilization of cubic lithium-stuffed garnets of the type "Li7La3Zr2O12" by addition of gallium*. *Journal of power sources*, 2013. **225**: p. 13-19.
74. Li, C., *Gallium Substitution in Zirconate-Based Fast Ionic Conducting Ceramics*. 2016.
75. Li, C., et al., *Ga-substituted Li7La3Zr2O12: An investigation based on grain coarsening in garnet-type lithium ion conductors*. *Journal of Alloys and Compounds*, 2017. **695**: p. 3744-3752.
76. Liu, Z., et al., *In situ X-ray photoelectron spectroscopy investigation of the solid electrolyte interphase in a Li/Li6.4Ga0.2La3Zr2O12/LiFePO4 all-solid-state battery*. *Journal of Solid State Electrochemistry*, 2019. **23**(7): p. 2107-2117.
77. Luo, Y., et al., *Electrochemical properties and structural stability of Ga- and Y- co-doping in Li7La3Zr2O12 ceramic electrolytes for lithium-ion batteries*. *Electrochimica Acta*, 2019. **294**: p. 217-225.
78. Rettenwander, D., et al., *A Synthesis and Crystal Chemical Study of the Fast Ion Conductor Li7-3xGaxLa3Zr2O12 with x = 0.08 to 0.84*. *Inorganic Chemistry*, 2014. **53**(12): p. 6264-6269.
79. Rettenwander, D., et al., *Site Occupation of Ga and Al in Stabilized Cubic Li7-3(x+y)GaxAlyLa3Zr2O12 Garnets As Deduced from 27Al and 71Ga MAS NMR at Ultrahigh Magnetic Fields*. *Chemistry of Materials*, 2015. **27**(8): p. 3135-3142.
80. Rettenwander, D., et al., *Structural and Electrochemical Consequences of Al and Ga Cosubstitution in Li7La3Zr2O12 Solid Electrolytes*. *Chemistry of Materials*, 2016. **28**(7): p. 2384-2392.
81. Wagner, R., et al., *Crystal Structure of Garnet-Related Li-Ion Conductor Li7-3xGaxLa3Zr2O12: Fast Li-Ion Conduction Caused by a Different Cubic Modification?* *Chemistry of Materials*, 2016. **28**(6): p. 1861-1871.
82. Wu, J.-F., et al., *Gallium-Doped Li7La3Zr2O12 Garnet-Type Electrolytes with High Lithium-Ion Conductivity*. *ACS Applied Materials & Interfaces*, 2017. **9**(2): p. 1542-1552.
83. Yang, T., et al., *The synergistic effect of dual substitution of Al and Sb on structure and ionic conductivity of Li7La3Zr2O12 ceramic*. *Ceramics International*, 2018. **44**(2): p. 1538-1544.
84. Cao, Z., et al., *Effect of Sb-Ba codoping on the ionic conductivity of Li7La3Zr2O12 ceramic*. *Ceramics International*, 2015. **41**(5, Part A): p. 6232-6236.

85. Barrow, N.S., *Homonuclear correlation in solid-state NMR: developing experiments for half-integer quadrupolar nuclei*. 2009, University of Warwick.
86. Zehe, C.S., R. Siegel, and J. Senker, *Solid-State NMR Spectroscopy: Introduction for Solid-State Chemists*. Handbook of Solid State Chemistry, 2017: p. 245-277.
87. Duer, M.J., *Introduction to solid-state NMR spectroscopy*. 2004: Blackwell Oxford.
88. Duer, M.J., *Solid state NMR spectroscopy: principles and applications*. 2008: John Wiley & Sons.
89. Huff, L.A., et al., *Identification of lithium–sulfur battery discharge products through 6Li and 33S solid-state MAS and 7Li solution NMR spectroscopy*. Surface Science, 2015. **631**: p. 295-300.
90. Bottke, P., et al., *Ion Dynamics in Solid Electrolytes: NMR Reveals the Elementary Steps of Li^+ Hopping in the Garnet $\text{Li}_6.5\text{La}_3\text{Zr}_1.75\text{Mo}_0.25\text{O}_{12}$* . Chemistry of Materials, 2015. **27**(19): p. 6571-6582.
91. Spencer, T., et al., *Structural Complexity and Electrical Properties of the Garnet-Type Structure $\text{LaLiO}_3\text{FeO}_2$ Studied by 7Li and 139La Solid State NMR Spectroscopy and Impedance Spectroscopy*. Chemistry of Materials, 2011. **23**(12): p. 3105-3113.
92. Cao, F., et al., *A novel and safety lithium thermal battery electrolyte - $\text{Li}_7\text{La}_3\text{Zr}_2\text{O}_{12}$ prepared by solid state method*. Solid State Ionics, 2018. **326**: p. 131-135.
93. Loho, C., et al., *Garnet-Type $\text{Li}_7\text{La}_3\text{Zr}_2\text{O}_{12}$ Solid Electrolyte Thin Films Grown by CO_2 -Laser Assisted CVD for All-Solid-State Batteries*. Journal of The Electrochemical Society, 2016. **164**(1): p. A6131-A6139.
94. Tsai, C.-L., et al., *$\text{Li}_7\text{La}_3\text{Zr}_2\text{O}_{12}$ Interface Modification for Li Dendrite Prevention*. ACS Applied Materials & Interfaces, 2016. **8**(16): p. 10617-10626.
95. Tan, J. and A. Tiwari, *Characterization of $\text{Li}_7\text{La}_3\text{Zr}_2\text{O}_{12}$ Thin Films Prepared by Pulsed Laser Deposition*. MRS Proceedings, 2012. **1471**: p. mrrs12-1471-yy03-04.
96. Jin, Y. and P.J. McGinn, *$\text{Li}_7\text{La}_3\text{Zr}_2\text{O}_{12}$ electrolyte stability in air and fabrication of a $\text{Li}/\text{Li}_7\text{La}_3\text{Zr}_2\text{O}_{12}/\text{Cu}_0.1\text{V}_2\text{O}_5$ solid-state battery*. Journal of Power Sources, 2013. **239**: p. 326-331.
97. Uddin, M.-J. and S.-J. Cho, *Reassessing the bulk ionic conductivity of solid-state electrolytes*. Sustainable Energy & Fuels, 2018. **2**(7): p. 1458-1462.
98. Huggins, R.A., *Simple method to determine electronic and ionic components of the conductivity in mixed conductors a review*. Ionics, 2002. **8**(3): p. 300-313.
99. Zhang, Y., et al., *Field assisted sintering of dense Al-substituted cubic phase $\text{Li}_7\text{La}_3\text{Zr}_2\text{O}_{12}$ solid electrolytes*. Journal of Power Sources, 2014. **268**: p. 960-964.
100. Kokal, I., et al., *Sol–gel synthesis and lithium ion conductivity of $\text{Li}_7\text{La}_3\text{Zr}_2\text{O}_{12}$ with garnet-related type structure*. Solid State Ionics, 2011. **185**(1): p. 42-46.
101. Shao, C., et al., *Structure and ionic conductivity of cubic $\text{Li}_7\text{La}_3\text{Zr}_2\text{O}_{12}$ solid electrolyte prepared by chemical co-precipitation method*. Solid State Ionics, 2016. **287**: p. 13-16.
102. Pesci, Federico M., et al., *Elucidating the role of dopants in the critical current density for dendrite formation in garnet electrolytes*. Journal of Materials Chemistry A, 2018. **6**(40): p. 19817-19827.
103. Langer, F., et al., *Impedance Spectroscopy Analysis of the Lithium Ion Transport through the $\text{Li}_7\text{La}_3\text{Zr}_2\text{O}_{12}/\text{P}(\text{EO})_{20}\text{Li}$ Interface*. Journal of The Electrochemical Society, 2017. **164**(12): p. A2298-A2303.
104. He, L., et al., *A new approach for synthesizing bulk-type all-solid-state lithium-ion batteries*. Journal of Materials Chemistry A, 2019. **7**(16): p. 9748-9760.
105. Randles, J.E.B., *Kinetics of rapid electrode reactions*. Discussions of the Faraday Society, 1947. **1**(0): p. 11-19.
106. Wang, D., et al., *Toward understanding the lithium transport mechanism in garnet-type solid electrolytes: Li^+ ion exchanges and their mobility at octahedral/tetrahedral sites*. Chemistry of Materials, 2015. **27**(19): p. 6650-6659.

107. Irvine, J.T., D.C. Sinclair, and A.R. West, *Electroceramics: characterization by impedance spectroscopy*. Advanced materials, 1990. **2**(3): p. 132-138.
108. Hummel, R.E., *Electronic Properties of Materials*. Springer New York.
109. Sun, C., et al., *Recent advances in all-solid-state rechargeable lithium batteries*. Nano Energy, 2017. **33**: p. 363-386.
110. Deviannapoorani, C., et al., *Lithium ion transport properties of high conductive tellurium substituted Li₇La₃Zr₂O₁₂ cubic lithium garnets*. Journal of Power Sources, 2013. **240**: p. 18-25.
111. Jin, Y. and P.J. McGinn, *Al-doped Li₇La₃Zr₂O₁₂ synthesized by a polymerized complex method*. Journal of Power Sources, 2011. **196**(20): p. 8683-8687.
112. Dumon, A., et al., *High Li ion conductivity in strontium doped Li₇La₃Zr₂O₁₂ garnet*. Solid State Ionics, 2013. **243**: p. 36-41.
113. Takano, R., et al., *Low temperature synthesis of Al-doped Li₇La₃Zr₂O₁₂ solid electrolyte by a sol-gel process*. Solid State Ionics, 2014. **255**: p. 104-107.
114. Murugan, R., S. Ramakumar, and N. Janani, *High conductive yttrium doped Li₇La₃Zr₂O₁₂ cubic lithium garnet*. Electrochemistry Communications, 2011. **13**(12): p. 1373-1375.
115. Wang, D., et al., *The synergistic effects of Al and Te on the structure and Li⁺-mobility of garnet-type solid electrolytes*. Journal of Materials Chemistry A, 2014. **2**(47): p. 20271-20279.
116. Meesala, Y., et al., *An efficient multi-doping strategy to enhance Li-ion conductivity in the garnet-type solid electrolyte Li₇La₃Zr₂O₁₂*. Journal of Materials Chemistry A, 2019. **7**(14): p. 8589-8601.
117. Il'ina, E., A. Raskovalov, and A. Safronov, *The standard enthalpy of formation of superionic solid electrolyte Li₇La₃Zr₂O₁₂*. Thermochemica Acta, 2017. **657**: p. 26-30.
118. Bloembergen, N., E.M. Purcell, and R.V. Pound, *Relaxation effects in nuclear magnetic resonance absorption*. Physical review, 1948. **73**(7): p. 679.
119. Küchler, W., et al., *⁷Li NMR relaxation by diffusion in hexagonal and cubic Li_xTiS₂*. Solid State Ionics, 1994. **70**: p. 434-438.
120. Wagner, R., et al., *Fast Li-Ion-Conducting Garnet-Related Li_{7-3 x Fe x La₃Zr₂O₁₂ with Uncommon I 43 d Structure}*. Chemistry of Materials, 2016. **28**(16): p. 5943-5951.